ξ Tauri: a unique laboratory to study the stellar and dynamical evolution of a multiple system

J.A. Nemravová[1], P. Harmanec[1], C.T. Bolton[2], H. Božić[3], M. Brož[1], L.S. Buda[14], C. Cameron[4], R. Chini[14], S. Engle[5], J.H. Grunhut[6], T. Dembsky[14], D.B. Guenther[7], E.F. Guinan[5], C.A. Hummel[6], D. Korčáková[1], P. Koubský[8], R. Kuschnig[9], R. Kříček[1], J.M. Matthews[4], P. Mayer[1], G.P. McCook[5], A.F.J. Moffat[10], D. Mourard[11], A. Prša[5], J. Ribeiro[12], J. Rowe[13], S. Rucinski[2], P. Rutsch[1], M. Šlechta[8], D. Vokrouhlický[1], V. Votruba[8], W.W. Weiss[9], M. Wolf[1], P. Zasche[1], and the CHARA/VEGA and NPOI teams

1. Astronomical Institute of the Charles University, Faculty of Mathematics and Physics,
   V Holešovičkách 2, CZ-180 00 Praha 8 - Troja, Czech Republic
2. David Dunlap Observatory, University of Toronto, P.O. Box 360, Richmond Hill, ON, L4C 4Y6s, Canada
3. Hvar Observatory, Faculty of Geodesy, Zagreb University, Kačićeva 26, 10000 Zagreb, Croatia
4. Department of Physics & Astronomy, University of British Columbia, 6224 Agricultural Road, Vancouver, British Columbia,
   V6T 1Z1 Canada
5. Department of Astronomy and Astrophysics, Villanova University, Villanova, PA 19085, USA
6. European Southern Observatories, Karl–Schwarzschild–Str. 2, 85748 Garching bei München, Germany
7. Department of Astronomy and Physics, Saint Mary's University, Halifax, N.S., B3H 3C3, Canada
8. Astronomical Institute, Academy of Sciences of the Czech Republic, 251 65 Ondřejov, Czech Republic
9. Institute of Astronomy, University Vienna, Türkenschanzstrasse 17, A-1180 Vienna, Austria
10. Département de physique, Université de Montréal, C.P. 6128, Succ. Centre-Ville, Montréal, QC H3C 3J7, and Observatoire du
    mont Mégantic, Canada
11. Laboratoire Lagrange, OCA/UNS/CNRS UMR7293, BP4229, 06304 Nice Cedex, France
12. Observatório do Instituto Geográfico do Exército, R. Venezuela 29 3 Esq., 1500-618, Lisbon, Portugal
13. NASA Ames Research Center, Moffett Field, CA 94035, USA; SETI Institute, Mountain View, CA 94043, USA
14. Astronomisches Institut, Ruhr-Universität Bochum, Universitätsstraße 150, D-44780, Bochum, Germany

Release June 26, 2015

ABSTRACT

to be developed

Key words. Stars: binaries:close – Stars: binaries: spectroscopic – Stars: fundamental parameters – Stars: individual: ξ Tau

1. Introduction

The naked-eye star ξ Tau (2 Tau, HD 21364, HIP 16083, HR 1038) is a hierarchical quadruple system, consisting of two sharp-lined A stars, which undergo binary eclipses, a more distant broad-lined B star and a much more distant F star. The visual magnitude $V = 3^m72$, the declination of $9°44'$, and quite accurate Hipparcos parallax 15.6 ± 1.04 mas (van Leeuwen 2007) make ξ Tau an easy and interesting target for a wide range of instruments and observational techniques.

The binary nature of the system was discovered by Campbell (1909). The wide orbit was first resolved by Mason et al. (1999) via speckle interferometry. All later available speckle-interferometric observations were analysed by Rica Romero (2010), who derived an orbital period of 52 ± 15 yrs, eccentricity 0.568 ± 0.77, longitude of periastron $3°0 \pm 6°3$, and the angular semi-major axis $0''441 \pm 0''027$. The inner triple system was first mentioned by Fekel (1981), who quoted orbital periods of 7^d15 and 145^d0 based on a private communication from Dr. C.T. Bolton. The orbital elements of the triple subsystem

were published in a catalogue by Tokovinin (1997). More accurate elements were given in a preliminary report by Bolton & Grunhut (2007), who obtained periods of $7^d1466440(49)$ and $145^d1317(40)$, the eccentricity of the outer orbit being 0.149. They were also first to note that the inner binary is an eclipsing system, based on Hipparcos photometry. Hummel et al. (2013) reported a preliminary interferometric orbit of the 145^d2 system. The first detailed, although still preliminary study of ξ Tau was published by Nemravová et al. (2013). These authors analysed numerous spectral, photometric and interferometric observations and discovered the presence of apsidal motion of the 145^d2 orbit with an apsidal period of 224 ± 147 yrs. They were able to disentangle the spectra of both A stars and the broad-lined B star but found no evidence of the faint F spectrum in their red spectra.

In the following text we shall denote the individual components and orbits of the system as follows: Components Aa and Ab are the primary and secondary of the close eclipsing subsystem revolving in a 7.15-d orbit 1. Component B is the broad-lined star of spectral type B, revolving with the close pair in the 145-d orbit 2. Finally, we denote the faint and very distant F-type star as component C and its 51-yr orbit with the triple subsystem as orbit 3.

The paper is organized as follows: The description of the available observational material is in the Section 2. Analyses of individual types of observations is discussed in the next three sections: Spectroscopy (Section 3), photometry (Section 4), and spectro-interferometry (Section 5). Finally, the improved physical properties of the system, based on the integrated results from the previous sections are presented in Section 6.

2. Observations and reductions

The system was observed with three different methods each allowing the determination of a slightly different set of properties of the systems. The three methods are: 1) the spectroscopy, 2) the photometry and 3) the spectro-interferometry. Only basic characteristics of the observational material is given in following paragraphs a more detailed description on the reduction procedure is given in the Appendix A. Please, note that throughout this paper we use a simplified form of heliocentric Julian dates RJD = HJD − 2400000.0.

2.1. The spectroscopy

The series of spectroscopic observations used by Nemravová et al. (2013) was complemented with new slit CCD spectra secured in the coudé focus of the Ondřejov 2 m telescope, Czech Republic, echelle CCD spectra obtained with the FEROS spectrograph (Kaufer et al. 1999) attached to the ESO/MPG 2.2 m telescope at La Silla, Chile and echelle CCD spectra from the BESO spectrograph attached to the 1.5 m hexapod telescope (Steiner et al. 2008) at Cerro Amazones, Chile. Two additional echelle spectra were extracted from the ELODIE spectrograph archive (Moultaka et al. 2004). The journal of all available spectra is in Table 2.1. The spectroscopic observations from individual instruments were treated as having different systemic velocities to account for possible slight zero-point velocity shifts between them.

Radial velocities (RVs) were measured in the fully reduced and normalized spectra (see Appendix ... for details on the reductions) using an automatic method based on minimization of squared difference between the observed spectrum and a set of template spectra, each representing a component of the multiple system multiplied by its fractional luminosity and shifted in RV. The sum of squares subjected to minimization procedure is

$$\chi^2\left(RV_j\right) = \sum_{i=1}^{N\lambda} \left(\frac{I_{\mathrm{OBS}}\left(\lambda_i\right) - \sum_{j=1}^{\mathrm{NC}} I_{\mathrm{TEM}}\left(\lambda_i, RV_j\right)}{\sigma_i} \right)^2, \quad (1)$$

where $I_{\mathrm{OBS}}\left(\lambda_i\right)$ (I_{TEM}) is the relative flux of the i-th point of the observed (template) spectrum, $N\lambda$ is the length of the spectrum, NC is the number of components and RV_j the radial velocity of the j-th component. In early attempts, synthetic spectra were used as templates, but once a disentangled component spectra were obtained we used them, since they provide a more accurate RV determination especially during conjunctions. (Note a discussion on this topic in Harmanec et al. (2015), who arrived at the same conclusion for the 2-D cross-correlation RV measurements.) The adopted approach forced us, however, to measure RVs from the echelle spectra only in the wavelength intervals that are available for the slit spectra, since (1) only for them the disentangled profiles were obtained, and (2) the fractional luminosity of each component is also function of the wavelength, hence the compared bands should not exceed several tens of nm. We were able to disentangle spectra in the following spectral regions $\Delta\lambda_{\mathrm{disentangled}} =$

$\{4450 - 4510, 4775 - 4975, 6330 - 6710\}$ Å. In these bands prominent spectral lines and their close surroundings were fitted. The global minimum of Eq. 1 was determined with the simulated annealing method (Kirkpatrick et al. 1983) and once found, the bottom of it was found with the simplex method (Nelder & Mead 1965). The uncertainty of the measured RVs was estimated using a Monte Carlo simulation. For each observed spectrum the standard deviation σ_{CF} of the relative flux in the continuum was estimated. A new "observed" was then created by drawing random numbers from a Gaussian distribution centred at the flux of the original spectrum and standard deviation equal to σ_{CF}. The RVs were then measured on this simulated "observed" spectrum. The procedure was then repeated five hundred times for each observed spectrum. The uncertainty of the RVs measured on the original spectra was estimated from the distribution of the RVs measured in the simulated spectra. Correlations between the RVs were inspected and were found uncorrelated with the exception of eclipses, when the RVs of components Aa and Ab were strongly correlated.

2.2. The photometry

Photometric observations used by Nemravová et al. (2013) were complemented by a new set of highly precise observations acquired with the satellite MOST (Walker et al. 2003), with another series of Johnson UBV and $UBVR$ observations secured at Hvar. Additionally, we also used the photometric minima published by Zasche et al. (2014). A journal of all available photometric observations is in Table 2.

The satellite MOST monitored ξ Tau over 16 days almost continuously. It acquired 21525 observations, but the light curve still contained a large number of outliers after the initial reductions. A low-passband Butterworth filter (Butterworth 1930) was applied to obtain cleaner mean light curve. We computed the standard deviation of all points σ_{MOST} around the mean curve and then removed all points, which deviated for more than $2.5\sigma_{\mathrm{MOST}}$ from the mean light curve. After this procedure several outliers remained and those were removed manually after a visual inspection. All observations secured before RJD = 56522 were removed, since the instrument had not been relaxed properly and was affecting the measurements in a non-homogeneous way. The remaining 18510 observations were then subjected to analyses.

2.3. The spectro-interferometry

THE DESCRIPTION OF THE OBSERVATIONAL MATERIAL FROM NPOI IS MISSING. WILL BE DONE BY CH. The ξ Tau system was observed with the VEGA spectro-interferometer (Mourard et al. 2009) mounted on the CHARA telescope array (ten Brummelaar et al. 2005). The observations were carried out during two runs in 2011 and in 2012. A preliminary analysis of the observations obtained during the first run has already been published by Nemravová et al. (2013), but only very briefly. Therefore, we also describe these observations here. In the description of the reduction procedure we will focus on the second run, but the procedure was virtually the same for the first run.

Five observations were acquired in 2011. All observations were taken in the 3-telescope (3T) mode and included the CHARA baselines E1E2W2, W1W2S2, W2E2S2, ranging from 63 m to 245 m (symbols E1, E2, S1, S2, W1, W2 denoting the telescopes in the CHARA telescope array). Ten new observa-

Table 1. Journal of spectroscopic observations and radial velocities. Individual files are sorted according to the time of the first observation. For each dataset N denotes the number of usable spectra for components Aa, Ab, and B, the spectral resolution is a two-pixel resolution rounded to hundreds.

Instrument	γ No.	Time interval (RJD)	N Aa/Ab/B	Wavelength range (Å)	Spectral resolution
a	01	49300.7–52670.5	37/37/37	4357–4568	10800
b	02	51960.3–53637.6	04/04/04	4270–4523	42000
b	02		04/04/04	4759–4991	
b	02		04/04/04	6260–6735	
c	05	55041.9–55867.6	13/13/13	4270–4523	48000
c	05		13/13/13	4759–4991	
c	05		13/13/13	6260–6735	
d	03	55579.4–56357.3	34/34/34	4270–4523	19200
d	03	56579.4–56889.6	05/04/05	4274–4508	19200
d	03	55579.3–55645.3	02/02/02	4378–4632	17700
d	03	55579.3–56357.3	20/20/20	4753–5005	19300
d	03	56527.6–56592.5	05/05/05	4759–4991	21500
d	03	56527.6–56889.6	14/14/14	6260–6735	14000
d	03	55561.3–56357.3	58/58/59	6255–6767	12700
e	03	55597.4–55980.3	19/19/22	6497–6688	14000
f	04	56555.7–56564.7	12/12/12	4270–4523	48000
f	04		12/12/12	4759–4991	
f	04		12/12/12	6260–6735	

Notes. Instruments used: a... Cassegrain slit spectrograph attached to the 1.88 m reflector of the David Dunlap Observatory; b... Elodie echelle spectrograph, 1.93 m reflector of the Haute Provence Observatory, full wavelength range of 4000–6800 Å; c... BESO echelle spectrograph, Cerro Armazones Observatory 1.5 m hexapode reflector, full wavelength range of 3527–8860 Å; d... coudé slit spectrograph, Site... and ...detectors, Ondřejov 2.0 m reflector; e... Littrow LHIRESIII slit spectrograph, 0.356 m reflector of the Military Geographical Institute of Lisboa; f... Feros echelle spectrograph, La Silla 2.20 m reflector, full wavelength range 3527–9217 Å.

Table 2. Journal of photometric observations. For each dataset N is the number of observations.

Dataset	N	Time interval	Passbands	Comp / Check	Observatory
01	429/439/440+	46324.6–55945.3[a]	UBV	4 Tau / 6 Tau	HVAR
61	69	47909.6–48695.0	V[b]	all-sky	HIPP
11	26	55569.3–55579.4	UBV	6 Tau / 4 Tau	SAAO
16	131/133/135	55883.9–55956.8	UBV	4 Tau / 6 Tau	VILL
61	18510	56222.0–56238.0	$Most$	all-sky	MOST
01	12	56520.6–56882.6	$UBVR$	4 Tau / 6 Tau	HVAR

Notes. *Abbreviations used for individual observatories and instruments:* HVAR - 0.65 m reflector of the Hvar Observatory, Croatia, photoelectric photometer with an EMI 6256 tube; HIPP - 0.29 m reflector of the Hipparcos Space Observatory, CCD detector; SAAO - 0.50 m reflector of the South African Astronomical Observatory, South Africa, with a Hammamatsu tube and photon-counting photometer; VILL - Villanova Observatory, USA, Automatic Photometric Telescope (APT), photoelectric photometer; UHL - Private Observatory of R. Uhlář, CCD camera; MOST - 0.15 m reflector of the MOST satellite, CCD detector. [a] Only three observations were taken before RJD=54116, all at RJD 46324. [b] The original Hipparcos $H_{\rm p}$ broad-band observations were transformed to Johnson V filter after Harmanec (1998). Note, however, that for the light-curve solutions, the limb darkening corresponding to the original passband was used.

tions were secured in 2012. Four of them were taken in the 3T mode and the remaining six were taken in the 2-telescope (2T) mode. The 2T observations included the CHARA baselines E2E1 and S2S1, their projections ranging from 34 m to 66 m. The 3T observations contained the E2E1W2 and W2W1S1 baselines ranging from 65 m to 279 m. A journal of all interferometric observations is in Table 3.

The observations were obtained with two detectors centred at 535 nm (denoted BLUE) and 730 nm (denoted RED) at spectral resolution of R ~6000. Individual frames were recorded with a frequency 100 Hz and grouped into blocks containing 2500 frames. Each block was coherently summed up and each observation consists of 20–90 of such blocks. Two

20 nm wide bands were chosen in the BLUE region and two 30 nm wide bands in the RED one. The four bands used are $\Delta\lambda_{\rm IF} = \{532 - 552, 540 - 560, 700 - 730, 730 - 760\}$ [1] The signal was summed up within these bands and the instrumental squared visibility $V_{\rm INST}$ was derived for the sum. The spectral bands have to be narrow because of a slight curvature of the spectrum recorded on the detector would cause de-coherence. All bands are very narrow, therefore the de-coherence caused by the usage of a polychromatic light is negligible. There are no strong

---

[1] The only difference between the reduction procedure of the observations acquired in 2011 and 2012 is in the choice of the spectral bands. The following bands were used in 2011 $\Delta\lambda_{\rm IF(OLD)} = \{535 - 545, 545 - 560, 700 - 720, 710 - 730, 720 - 740\}$ nm.

Table 3. Journal of the spectro-interferometric observations of ξ Tau. Symbols ϕ_A and ϕ_B denote the orbital phase of the eclipsing binary, and of the tertiary, respectively, B the mean length of the projected baseline, θ the position angle of the projected baseline. The calibrators used are identified in column "Cal.: as follows: 1... HD 21686, 2... HD 18604, and 3... HD 26793.

RJD	NB	ϕ_A	ϕ_B	B (m)	θ (deg)	Cal.
The 2011 run						'
55825.8907	3-1	0.193	0.488	064.6	-155.9	1,2
	3-2			150.0	-160.6	1,2
	3-3			217.2	-158.9	1,2
55846.8703	3-1	0.129	0.633	065.8	-154.2	2
	3-2			155.8	-159.3	2
	3-3			221.4	-157.8	2
55850.8130	3-1	0.680	0.660	147.0	-160.9	1,2
	3-2			154.1	-090.1	1,2
	3-3			244.8	+056.0	1,2
55854.8645	3-1	0.247	0.688	065.6	-153.1	1,2
	3-2			156.2	-158.3	1,2
	3-3			221.6	-156.8	1,2
55854.9548	3-1	0.260	0.688	135.3	-148.5	1,2
	3-2			172.7	-057.7	1,2
	3-3			217.7	+084.1	1,2
55856.8928	3-1	0.531	0.702	063.3	-149.9	2,3
	3-2			152.5	-155.6	2,3
	3-3			216.3	-154.2	2,3
The 2012 run						
56194.8118	2-1	0.814	0.029	054.8	-156.0	1
56194.9180	2-1	0.829	0.030	065.9	-154.1	1
56197.8894	3-1	0.245	0.050	065.6	-155.2	1
	3-2			153.5	-160.1	1
	3-3			218.7	-158.6	1
56197.9362	3-1	0.252	0.051	065.0	-152.1	1
	3-2			155.6	-157.5	1
	3-3			220.4	-155.9	1
56200.0052	3-1	0.541	0.065	106.3	-002.5	1
	3-2			203.9	-060.1	1
	3-3			276.1	-041.1	1
56200.0306	3-1	0.545	0.065	099.2	-000.3	1
	3-2			207.7	-056.8	1
	3-3			278.3	-039.2	1
56226.9927	2-1	0.317	0.251	045.4	-125.8	1
56227.0299	2-1	0.323	0.251	040.0	-109.9	1
56227.8758	2-1	0.441	0.257	031.3	+100.3	1
56227.9720	2-1	0.454	0.258	033.4	+117.0	1

Notes. Ephemeris, which was used to compute the orbital phases: A - $T_{min}^A = 7.1467 \times E+$, B - $T_{per}^B = 145.17 \times E+$, where E is the epoch, T_{min}^A the epoch of the primary minimum of the eclipsing binary, T_{per}^B the epoch of the periastron passage of the outer orbit.

Table 4. Properties of calibrator stars HD 21686, HD 18604. T_{eff} is the effective temperature, g the gravitational acceleration, UDV (UDR) the uniform disk diameter for the filter V (R) of the Johnson photometric system, m_V (m_R) magnitude of the calibrator in the Johnson V (R) filter. They were adopted from Lafrasse et al. (2010).

Parameter Calibrator	Unit	Value		
		HD 21686	HD 18604	HD 26793
Spectra type		A0V	B6III	B9Vn
T_{eff}	(K)	9790	13000	10500
$\log g_{[cgs]}$		4.1	3.4	4.0
m_V	(mag)	5.125	4.703	5.210
m_R	(mag)	5.087	4.730	5.194
UDV	(mas)	0.245(18)	0.257(18)	0.207(15)
UDR	(mas)	0.247(18)	0.257(18)	0.209(15)

mental visibility was estimated according to formula:

$$V^2_{\text{SCI}-\text{CAL}}(u,v) = V^2_{\text{SCI}-\text{INST}} \frac{V^2_{\text{CALIBRATOR}-\text{UD}}}{V^2_{\text{CALIBRATOR}-\text{INST}}}(u,v), \quad (2)$$

where $V^2_{\text{SCI}-\text{CAL}}$ is the calibrated visibility of ξ Tau, $V^2_{\text{SCI}-\text{INST}}$ the instrumental visibility of ξ Tau, $V^2_{\text{CALIBRATOR}-\text{UD}}$ the visibility of an uniform disk with a diameter listed in Table 4, and $V^2_{\text{CALIBRATOR}-\text{INST}}$ the instrumental visibility of a calibrator. In order to avoid inaccurate observations we removed all blocks having S/N<2 and whose optical path delay (OPD) differs from the mean OPD by more than 2σ. Such blocks usually represent only a random noise rather than a physical signal. In rare cases, when the instrumental visibility of ξ Tau was close to zero, but safely detected, and there was no suitable observation of a calibrator, the instrumental visibilities of ξ Tau were fitted as if they were calibrated, but they were assigned an error $\Delta V^2 = 0.05$. This admittedly incorrect procedure allowed us to save more usable observations for very long baselines.

3. Spectroscopy

The spectral lines of all three components of the triple subsystem of ξ Tau are clearly seen in all available spectra. The fourth component C was not detected in any of the spectra at our disposal. The attempts to detect lines of component C were done with the spectral disentangling and comparison of the near infrared spectra with synthetic profiles.

Two different approaches to derive the orbital elements of the triple subsystem of ξ Tau were used. The first one was a direct analysis of RVs measured with the method described in Section 2.1. The second one was the spectral disentangling (Simon & Sturm 1994; Hadrava 1995). The two approaches were not fully independent of each other. The spectra were disentangled while we kept the mass ratios of orbits 1 and 2 fixed at the values obtained from the analysis of measured RVs, but these RVs were obtained using the disentangled profiles as the templates (see Section 2.1).

Additionally, we also derived the basic radiative properties of ξ Tau via fits of interpolated synthetic spectra to the observed and disentangled spectra.

3.1. Direct analysis of RVs

The measured RVs were fitted with a simple model, which takes the most pronounced dynamic effects of the dynamic interaction

stellar lines in any of the four spectral bands used, the spectral band $730 - 760$ nm being affected by the telluric water vapour lines, but even those are smeared out by the low resolution of the spectra.

A calibrator (i.e a star with known diameter) was observed before and after each observation of ξ Tau. Calibrators were chosen with the tool SearchCal (Bonneau et al. 2006) and their list along with their basic properties is given in Table 4. The instru-

between the four components into account. The two effects we considered are the apsidal advance of orbit 2, and the light-time (LITE) effect. The RVs of the j-th component RV_j were estimated from the standard formula for the orbital motion:

$$RV_{\mathrm{j}}(t) = \sum_i K_{\mathrm{i}} \left[\cos\left(\omega_{\mathrm{i}}(t) + v_{\mathrm{i}}(t)\right) + e_{\mathrm{i}} \cos\omega(t)_{\mathrm{i}} \right], \qquad (3)$$

the index i goes over those orbits of ξ Tau, which are relevant for the motion of the j-th component of the ξ Tau system, K_{i} the semiamplitude of the radial velocity curve, ω_{i} the longitude of periastron, v_{i} the true anomaly, e_{i} the eccentricity, and t is time. The LITE correction is computed Δt_{LITE} as follows:

$$\Delta_{\mathrm{LITE,j}}(t) = \sum_i \frac{P_i K_i \left(1 - e_i^2\right)^{\frac{3}{2}}}{2\pi c} \frac{\sin\left[\omega_i(t) + v_i(t)\right]}{1 + e_i \cos v_i(t)}, \qquad (4)$$

where the index i goes over those orbits, which are hierarchically above the one, which the j-th component lies in (i.e over those, which produce LITE), P is the orbital period, and c the speed of light. Otherwise the notation is the same as for the Equation 3. The longitude of periastron is a linear function of time $\omega_i(t) = \omega_i(t_0) + k_i^\omega (t - t_{0,i})$, where $t_{0,i}$ is the reference epoch, k_i^ω is the mean speed of the apsidal motion of the i-th component.

The listed parameters were optimized by minimization of the following χ^2:

$$\chi^2 = \sum_{k=1}^{N_{\mathrm{S}}} \sum_{j=1}^{N_{\mathrm{C}}} \sum_{i=1}^{N_{\mathrm{O}}} \frac{1}{\sigma_i} \left[RV_j^{\mathrm{OBS}}(t_i) - \right.$$
$$\left. - RV_j^{\mathrm{SYN}}(t_i - \Delta t_{\mathrm{LITE}}) - \gamma_k \right]^2, \qquad (5)$$

where the index k goes over N_{S} subsets of the measured RVs the index j over N_{C} components of the ξ Tau system for which RVs were measured, and the index i goes over N_{O} individual measurements of the radial velocity. σ denotes individual uncertainties of the RVs estimated with the procedure described in Section 2, RV^{OBS} the measured radial velocity, RV^{SYN} the synthetic radial velocity computed with Eq. 3 corrected for the LITE via Eq. 4, γ denotes the systemic velocity.

A Python script which minimizes the Equation 5 with the Sequential Least Squares (Kraft 1988) implemented within the SciPy library (jon 2001–) was written and used.

The measured RVs were divided into different subsets, based on their origin and spectral region. Also the RVs of component B were assigned a different subset than components Aa and Ab. This approach allows for the compensation of slightly different RV zero points of individual data sets. The disentangled spectra, which were used for measuring of the radial velocities, may not have exactly zero velocity and additional systematic velocity shifts may be introduced during the normalization of the observed and disentangled spectra. In total the radial velocities were split into 36 subsets and an individual γ velocity had to be fitted for each.

Any outliers were removed in a systematic way. After convergence was achieved, a mean scatter $\mathrm{rms}_{\mathrm{k,j}}$ of observed radial velocities around the synthetic radial velocity curve was computed for each component and each subset separately. All points which deviated for more than $3.\mathrm{rms}_{\mathrm{k,j}}$ from the model were removed from the respective dataset. The outliers were removed in four iterations. In datasets containing only a few data, the removal had to be done manually. The remaining 1433 RV measurements were then fitted with the model defined by Equations 3 and 4. Even after removal of outliers the reduced χ^2

Table 5. Orbital elements of orbit 3 based on a fit to astrometric measurements published in WDS. **ERRORS ARE MISSING!**

Element	Unit	Value
P	(d)	18738.53201 ± 0.000
T_{p}	(RJD-2400000)	54599.411 ± 0.000
e		0.572 ± 0.000
a	($''$)	0.4398 ± 0.000
i	(deg)	23.914 ± 0.000
ω	(deg)	6.257 ± 0.000
Ω	(deg)	109.9531 ± 0.000

(Equation 11 divided by degrees of freedom) was of an order of 10^1. This shows that the estimates of the uncertainty of the RVs with the method described in the Section 2 underestimates the total error, because it is unable to account for various systematic effects. Therefore additional weighting based on the scatter of individual datasets around the synthetic radial velocity curve was employed.

We were unable to measure RV of component C and, therefore to derive accurate characteristics of orbit 3, but this component should cause orbital RV variations of the tertiary Aa+Ab+B of $\approx 1.0\,\mathrm{km\,s^{-1}}$. These are not detectable given the accuracy of the observed RVs $\gtrsim 1\,\mathrm{km\,s^{-1}}$ (which are comparable to rms presented in Table 6). Component C should also manifest itself by LITE variations of an order $\approx 6.10^{-3}\,\mathrm{d}$. These variations are also below the accuracy of our measurements. Hence the fourth component is very unlikely to affect the final fit of the RVs. To verify this statement, two solutions were computed. The first one corresponds to a model consisting of three stars and the second one to a model consisting of four stars, with the elements of orbit 3 fixed at the values obtained from a fit to astrometric measurements published in the Washington Double Star Catalogue (WDS) Mason et al. (2001) with a program developed by PZ (see its description in **CITACE**). The orbital parameters corresponding to the least-square fit of the astrometry are listed in Table 5. The physical size of the semimajor axis of the triple subsystem was estimated using the Hipparcos parallax van Leeuwen (2007) and the estimate of the mass of component C $m_{\mathrm{C}} = 1.24\,\mathrm{M_\odot}$ based on Tokovinin (1997). Both solutions are presented in Table 6. A plot of the 3-star model and the measured radial velocities is shown in Figure 1. The reduced chi-square χ_{R}^2 of the two solutions presented in Table 6 shows that our measurements are not affected with the motion in orbit 3 or by LITE produced by this orbit.

3.2. Spectra disentangling

The disentangling of the studied spectra played essential role in our study since the disentangled profiles served as the template spectra for the RV determination and to the estimates of the radiative properties of the components. We were able to disentangle only the vicinity of four major spectral lines Hα, Hβ, He I 4471 Å&Mg II 4481 Å, and Hγ, since only these regions were available for both, the slit and echelle spectra. An attempt was made to disentangle the spectra of individual components using only the spectra from the three available echelle spectrographs. However, these disentangled spectra had strongly warped continua and were not useful for further investigation. The program KOREL (Hadrava 1995, 1997, 2009) (rel. 04-2004), which not only disentangles the spectra, but also fits the spectroscopic orbital parameters, was used. This gave us the op-

Table 6. Fits to the measured radial velocities. P_{AN} denotes the anomalistic period, T_{min} the epoch of the primary minimum of the light curve, T_p the epoch of the periastron passage. Orbital elements of orbit 3 were kept fixed at values given in Table 5.

Elements	Units				
Model		3-star		4-star	
Orbit		1	2	1	2
P_{AN}	(d)	7.14665 ± 0.00001	145.567 ± 0.044	7.14664 ± 0.00001	145.567 ± 0.021
T_{min}	(RJD)	56224.7056 ± 0.0017	–	56224.70537 ± 0.00088	–
T_p	(RJD)	–	55609.05 ± 0.48	–	55608.57 ± 0.21
K	(km s^{-1})	87.750 ± 0.19	37.78 ± 0.18	87.420 ± 0.095	37.910 ± 0.079
e		0.0^1	0.2212 ± 0.0048	0.0^1	0.2148 ± 0.0018
q		0.9478 ± 0.0034	1.084 ± 0.014	0.9421 ± 0.0015	1.0840 ± 0.0055
ω	(deg)	90^1	7.76 ± 1.28	90^1	6.52 ± 0.55
k^ω	(deg.yr^{-1})	0.0^1	2.74 ± 0.299	0.0^1	2.64 ± 0.15
rms	(km s^{-1})	1.69	2.75	1.76	2.77
		Systemic velocities			
$v_{\gamma,1}$	(km s^{-1})	09.40 ± 0.40		–	
$v_{\gamma,2}$	(km s^{-1})	06.08 ± 0.86		–	
$v_{\gamma,3}$	(km s^{-1})	-0.15 ± 0.27		–	
$v_{\gamma,4}$	(km s^{-1})	-3.54 ± 0.53		–	

Notes.
[1] The parameter was fixed.
K_1 refers to primary of the eclipsing binary K_{Aa}, and K_2 to the centre of gravity of the eclipsing binary K_{Aa+Ab}.
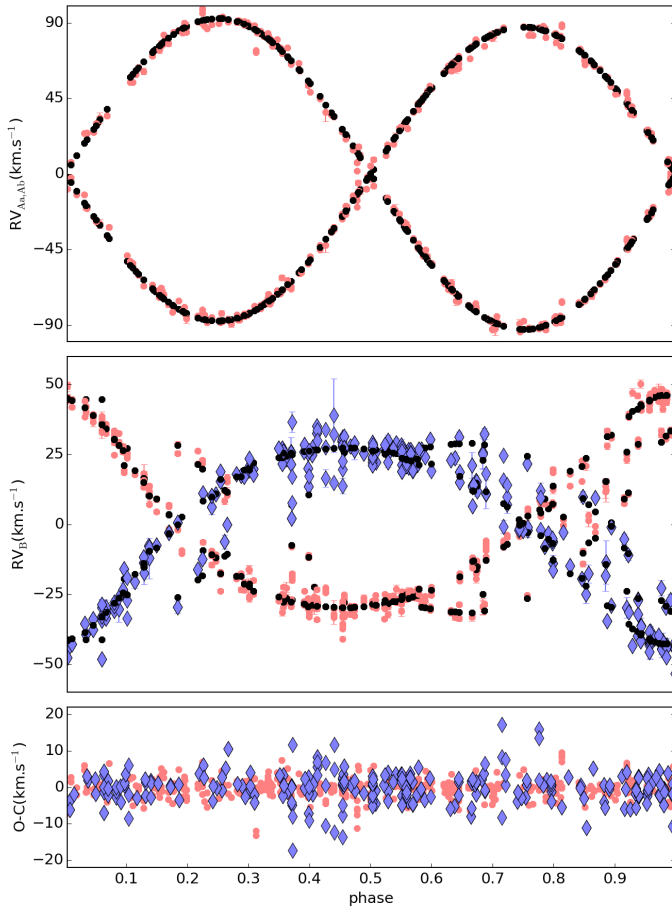
Fig. 1. Fit of the orbital model given by Eqs. 3, 4 to the measured RVs. Upper panel: RVs of components Aa and Ab in the centre of mass system of orbit 1, middle panel: RVs of component B in the centre of mass system of orbit 2, black points - RVs predicted by the model, bottom panel: OCs. Red points - RVs of components Aa, Ab, blue points - RVs of component B, black points - model RVs.

Table 7. Spectroscopic orbital solution obtained with the program KOREL. Notation is the same as in Table 6.

Element	Unit		
Orbit		1	2
P_{AN}	(d)	7.1467^1	145.571 ± 0.000
T_{min}	(RJD-56220)	4.7014 ± 0.0000	–
T_p	(RJD-56000)	–	9.204 ± 0.000
K	(km s^{-1})	87.957 ± 0.000	38.018 ± 0.000
e		0.000^1	0.196 ± 0.000
q		0.950^1	1.084^1
ω	(deg)	90.000^1	9.004 ± 0.000
k^ω	(deg.yr^{-1})	0.000^1	2.734 ± 0.000

Notes.
[1] The parameter was fixed.
MAPPING OF THE χ^2 NEEDED.
K_1 refers to primary of the eclipsing binary K_{Aa}, and K_2 to the centre of gravity of the eclipsing binary K_{Aa+Ab}.

portunity to compare the orbital solution obtained directly from the measured RVs with the result of KOREL.

The elements derived by Nemravová et al. (2013) served as initial estimates for the fitting. Several parameters were kept fixed, because they could be obtained with a higher precision by another method. Additionally, the mass ratio of both orbits q_1 and q_2 were fixed, because the analysis of the χ^2 minimized in KOREL (see Equation 4 in Hadrava 1997) has shown that the mass ratios are not well constrained. They were, therefore, adopted from the analysis of the measured RVs (see the preceding Section). **THE RESULT FROM JANA'S DIPLOMA THESIS, VERIFICATION OF THIS STATEMENT IS DESIRABLE.** The spectroscopic orbital elements obtained with KOREL are in Table 7. The disentangled profiles from the considered spectral regions are shown in Figure 3. As KOREL does not provide the uncertainties of the fitted elements, we mapped the sum of squares around the minima and estimated their errors from these maps. An attempt was car-

ried out to disentangle lines of component C in two spectral bands in the near infrared. The spectral bands were following $\Delta\lambda_{IR} = \{8570 - 8800, 7750 - 7800\}$ Å. Spectrum of component C was not detected in neither of these bands. It was probably due to relatively low S/N of the echelle spectra in the infrared region and their limited number.

3.3. Comparison of the observed and synthetic spectra

A program which interpolates in a grid of pre-calculated synthetic spectra was used to determine radiative properties of components of ξ Tau - the effective temperature T_{eff}, the logarithm of the gravitational acceleration, the projected rotational velocity $v \sin i$, the fractional luminosity L_R, the metallicity Z, and the radial velocity RV. A description of the program is given in Nasseri et al. (2014). In this application, the POLLUX grid (Palacios et al. 2010) was used for components B, Aa, Ab and the AMBRE grid de Laverny et al. (2012) for component C.

Disentangled spectra corresponding to the spectroscopic orbital solution listed in Table 7 were fitted. The disentangled spectra had to be re-normalized because they had slightly warped continua. The luminosity ratios are constant within the fitted spectral bands, hence the bands must be chosen narrow enough to satisfy this condition. [2] We were able to disentangle only three components of ξ Tau, but we also attempted to fit a composite spectrum consisting of four sets of spectral lines corresponding to each member of the system. Lines of component C were not detected this way. The best fit, whose parameters are listed within Table 8, is plotted in Figure 3. The uncertainties of the fitted elements were estimated with a Monte Carlo simulation. Each fitted parameter of the model was assigned a uniform prior probability distribution, Two hundred minimizations were run to sample the posterior probability distribution of the fitted parameters. The initial set of parameters was drawn from their an uniform prior probability distributions. The continuum S/N was estimated for each disentangled spectrum and it was used to add artificial noise on disentangled spectra before each individual minimization. The posterior distribution of the parameters was investigated. It can be roughly estimated with a Gaussian distribution around the minima. A strong correlations ($\gtrsim 0.95$) between the gravitational acceleration $\log g$ and the effective temperature T_{eff}, and between the gravitational acceleration $\log g$ and the projected rotational velocity $v \sin i$ of each component were found.

The fits also allowed to study the variations of the relative luminosities L_R of components Aa, Ab and B as a function of wavelength. The result could be compared to results from photometry and interferometry, where these values are also derived. Such a comparison is shown in Figure 2.

4. Photometry

The preliminary analysis published in Nemravová et al. (2013) has shown that the light variations can be attributed to the eclipses of the two components of orbit 1. Components Aa and Ab partially eclipse each other and produce two very narrow and nearly identical minima, which are only $\approx 0^m 1$ deep in the Johnson V passband.

The new highly accurate MOST satellite observations unveiled persistent low-amplitude rapid light oscillations, which are likely to be associated with component B. Besides it, the
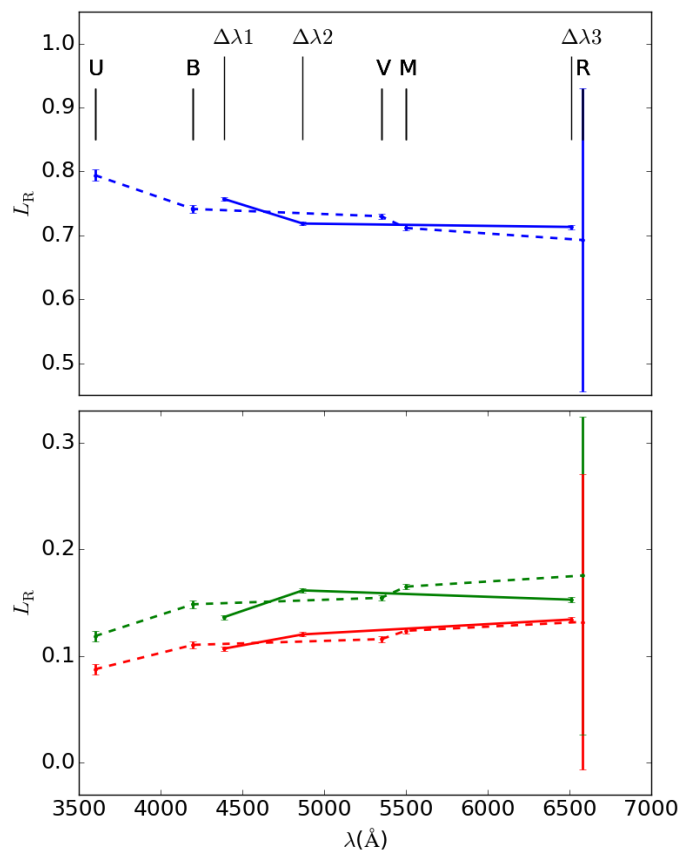

Fig. 2. A comparison of the fractional luminosities of the triple sub-system of ξ Tau. Full line connects luminosity fractions obtained by the fitting of the synthetic profiles to the disentangled ones, dashed line connects the luminosity fractions obtained from the modelling of the light curve. Labels above each point refer to spectral bands or filters from Tables 8 and 9. The wavelength of each point refers to the centre of the filter/spectral band. Blue colour = component C, green colour = component Aa red colour = component Ab.

MOST orbital light curves allow determination of very accurate radii of components Aa and Ab and a detection of variations of the mean motion of the eclipsing binary. Minima of the light curve and their surroundings acquired with the satellite MOST are shown in Figure 5.

4.1. The period analysis of the light curve

Our first goal in the analysis of the MOST light curve was to unveil the nature of the rapid cyclic low-amplitude changes. Two different methods were used to construct periodogram of the light curve. The first one is based on the Fourier transform (FT hereafter), and is implemented in the program `PERIOD04` (Lenz & Breger 2004). The other used the phase dispersion minimization technique (PDM) (Stellingwerf 1978) as implemented in the program `HEC27`[3]. The periodogram of the whole light curve is dominated by the orbital period of the eclipsing binary P_A. In order to study the rapid variations, having a full amplitude of only $\Delta m_M = 0^m 002$ in the MOST photometry, the time intervals covering the eclipses had to be removed. At first, a periodogram was constructed separately for each part of the light curve between the two minima. After verification

---

[2] It is possible to derive separate set of fractional luminosities for each spectral band.

[3] The program and a short user's guide are available at *http://astro.troja.mff.cuni.cz/ftp/hec/HEC27*.

Table 8. Parameters of the fit of the synthetic spectra to disentangled ones. The modelled spectral intervals were following $\Delta\lambda1 = \{4280-4400; 4455-4495\}$Å, $\Delta\lambda2 = \{4765-4975\}$Å, $\Delta\lambda3 = \{6325-6395; 6510-6620; 6655-6695\}$Å.

| Parameter | Unit | Value | | |
Component		B	Aa	Ab
T_{eff}	(K)	13920 ± 460	9700 ± 150	9580 ± 250
$\log g$	(cgs)	4.234 ± 0.080	4.411 ± 0.065	4.33 ± 0.10
$v\sin i$	(km s^{-1})	240.6 ± 5.9	23.0 ± 1.0	20.5 ± 1.2
RV	(km s^{-1})	7.10 ± 0.25	9.05 ± 0.16	9.42 ± 0.16
Z	(Z$_\odot$)	1.0^1	1.0^1	1.0^1
$L_{\text{R}}^{\Delta\lambda1}$		0.7571^2	0.1362 ± 0.0019	0.1067 ± 0.0018
$L_{\text{R}}^{\Delta\lambda2}$		0.7185^2	0.1614 ± 0.0021	0.1201 ± 0.0020
$L_{\text{R}}^{\Delta\lambda3}$		0.7132^2	0.1527 ± 0.0022	0.1341 ± 0.0027

Notes.
[1] The parameter was fixed.
[2] The luminosity of component B is constrained as follows: $L_{\text{R}}^{\text{B}} = 1.0 - L_{\text{R}}^{\text{Aa}} - L_{\text{R}}^{\text{Ab}}$.
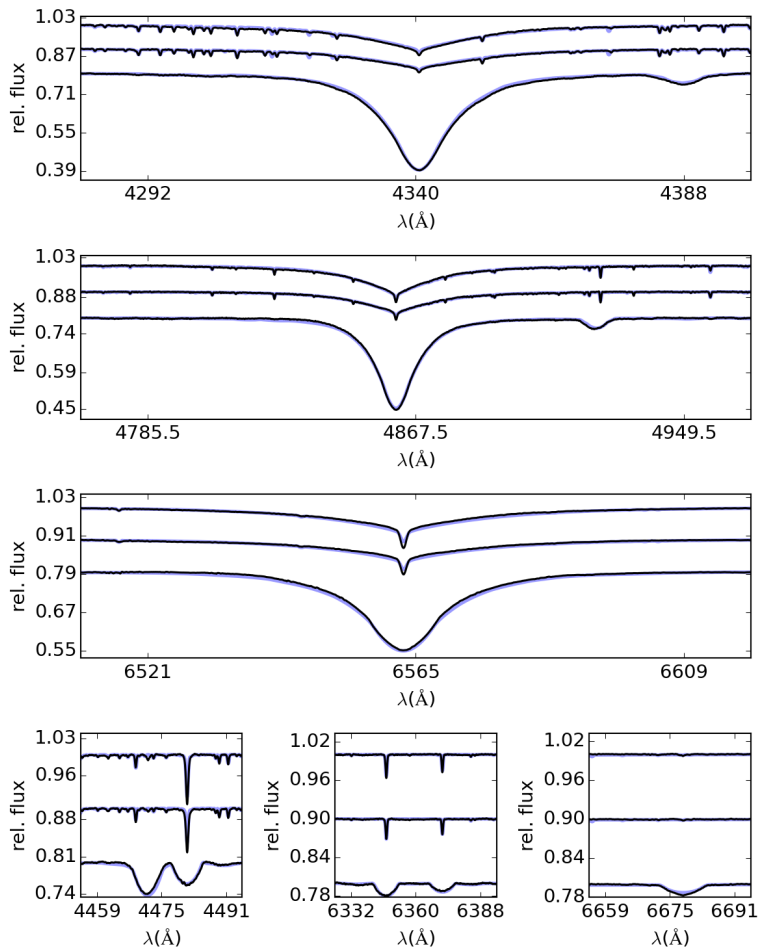
Fig. 3. A comparison of the disentangled and synthetic spectra. The fit corresponds to the parameters presented in Table 8. In each panel: top spectrum - component Aa, middle spectrum - component Ab, bottom spectrum - component B, thin black line - disentangled spectra, thick blue line - synthetic spectra.

that there are no major differences between these periodograms, a joint periodogram for all observations outside minima was computed. This periodogram gave a period of the rapid oscillations $P_{\text{R}1} = 0.424 \pm 0.005$. The character of the oscillations is reminiscent of a beat of two or more close periods. Hence we searched for another period in each subset. In four out of five subsets a period with significantly lower amplitude

of $P_{\text{R}2} = 0.357 \pm 0.030$ was detected, but it was identified as an alias of the period $P_{\text{R}1}$. Periodogram of the parts of the light curve outside the eclipses is in Figure 4. The two detected periods are marked with arrows.

Subsequently a period analysis of the whole set of photometric observations (both satellite and terrestrial) was done with both methods and it returned the optimal orbital period of
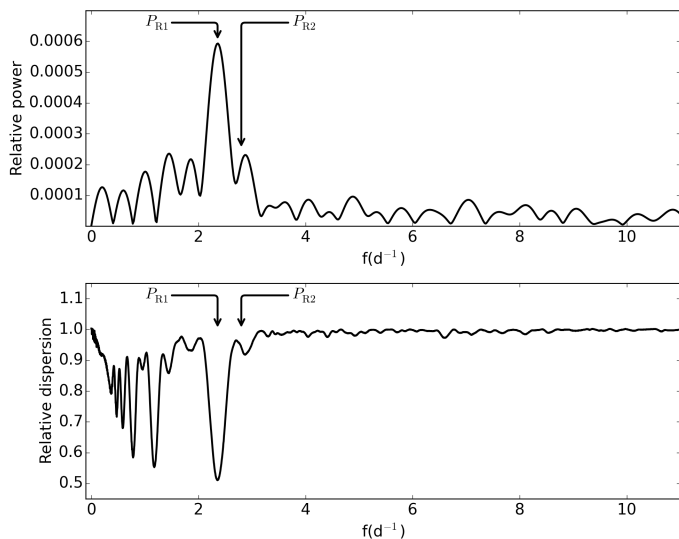
Fig. 4. Periodogram of the light curve acquired with the satellite MOST outside the eclipses. The two most prominent frequencies are marked with an arrow. The periodogram in the upper panel is a Fourier periodogram obtained with the program `PERIOD04` and the periodogram in the lower panel is the relative phase scatter obtained with program `HEC27`.
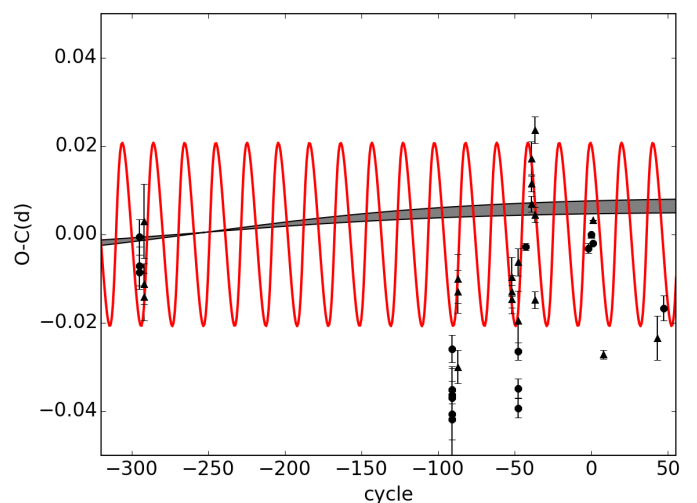

Fig. 6. The O-C diagram for the light curve minima of orbit 1. The orbit was assumed to be circular and the ephemeris $T_{\min} = 56224.7247 + 7.146646 \times E$ was adopted as the reference one. Black dots = delay of the primary minima, black triangles = delay of the secondary minima, grey field = the LITE from orbit 3 and its uncertainty and red line = model of the physical delay published by Rappaport et al. (2013).

$P_A =7.1467$ d, which practically the same as the period acquired from the fit of the radial velocities (see Table 6).

4.2. Model of the light curve

The light curve from the satellite MOST promised a precise determination of radii of both components of the eclipsing binary (Aa and Ab). Therefore it was studied at first separately from the rest of the observational material. In the next step it was complemented with ground-based observations. The program `PHOEBE` 1.0 (Prša & Zwitter 2005, 2006) was used to obtain the light-curve solution. The mass ratio q_A was taken from the analysis of the RVs (see Table 6). The eccentricity was initially assumed to be $e_A = 0.0$. The remaining parameters were adopted from Nemravová et al. (2013). The linear limb-darkening law was adopted and the coefficients were interpolated in a pre-calculated grid distributed along with `PHOEBE`. The bolometric albedos were taken from Claret (2001) and the gravity brightening coefficients from Claret (1998) for the corresponding temperatures of components of the eclipsing binary. The synchronicity ratio of both component was estimated to $F_{Aa} \simeq F_{Ab} = 3.3$ from the fit of the synthetic spectra to disentangled ones (see Table 8). Allowing only the fitting of the orbital inclination i_A, radii of both components R_{Aa}, R_{Ab} and the epoch of the primary minimum $T_{\min,A}$ a fit was computed. Surprisingly the orbital period of the eclipsing binary $P_A =7.14664$ d causes a small but clearly detectable shift $\Delta_{PHASE} \approx 0.0003$ between the two minima recorded with the satellite MOST. The shift disappears if the orbital period and the eccentricity is optimized. The local period and eccentricity which does not cause a phase shift between the two light curves acquired with satellite MOST are $P_A =7.14466$ d, $e_A \simeq 0.002$. A comparison of the two fits for (1) the circular orbit with the period taken from the model of the radial velocities, and (2) the eccentric-orbit solution with the locally derived period is in Figure 5. Especially the residuals from the two fits show that the global period P_1 introduces

a shift between the first and the second minimum recorded with the satellite MOST

An even larger phase shift $\Delta p \sim 0.004$ was detected if similar fit was computed for all available photometric observations. The difference between the global and the local period is large and cannot be attributed to the LITE from the fourth component (see the estimate of its magnitude in Section 3). This discovery led us to investigation of O-C variations across all available photometric observations. The photometry is unfortunately very sparse, therefore with the exception of the observations with the MOST satellite and light curves from amateur astronomers, observations from a larger time interval had to be combined. Observations covering a time interval of up to quarter of the orbital period of orbit 2 were combined, but typically the interval was $\lesssim 3P_1$.

The O-C diagram along with a model of the physical delay (see following paragraph) is plotted in Figure 6. The individual minima are shown in Figures B.1 and B.2. To estimate the epoch of each minimum a fit to all available photometric observations was computed. Then this model was fitted to individual minima, allowing only the convergence of the epoch of the minimum. The last primary minimum obtained with the satellite MOST and the period $P_1 =7.146646$ d were adopted as the reference ephemeris for the construction of the O-C diagram in Figure 6. The only exception are the observations acquired by amateur astronomers. These were not obtained in any filter so in those cases the epoch of the minimum was estimated with a parabola fit.

As already mentioned in Section 3 LITE produced by orbit 3 is too small to cause the detected O-C variations. A three-body integrations have shown that the O-C variations are likely caused by the dynamic interaction between the binary and the component B. The magnitude of the physical delay (nomenclature adopted from Rappaport et al. 2013) caused by the interaction was estimated with a model represented by Eq. (8) in Rappaport et al. (2013), which is based on the model published by Borkovits et al. (2003). A comparison of the model of the phys-
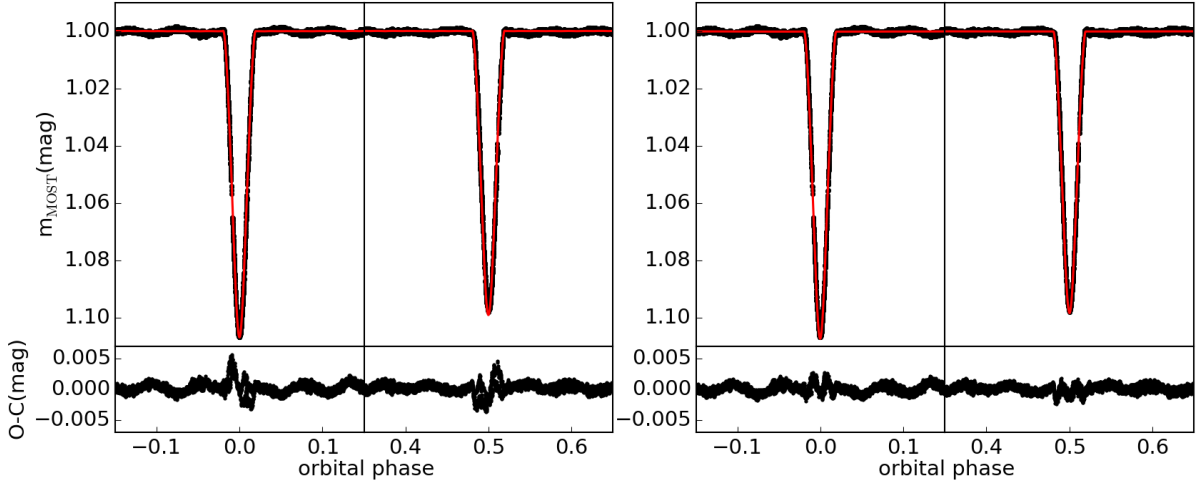
Fig. 5. Fit of the light curve from the satellite MOST. Only the light curve minima and their surroundings are shown. The primary (secondary) minimum is on the left (right) on each panel. The left panel corresponds to the circular solution $e_1 = 0.0$ and to orbital period $P = 7.14664$ d. The right panel corresponds to eccentric solution (solution no. 2 in Table 9). The observed light curve is plotted with black dots, the synthetic light curve with red line. Bellow each fit the residuals are plotted.

ical delay against measured O-C for all detected primary and secondary minima (see Figures B.1 and B.2) and the LITE produced by orbit 3 is shown in Figure 6.

Despite the facts that the light curve of ξ Tau is affected with the period changes and the low-amplitude variations we attempted to carry out a global fit of the light curve in all available filters with a model which does not account for either of those two effects in the program PHOEBE. Initial attempts to fit the whole dataset have returned the reduced χ^2 by almost two orders higher than the expected value. There are two possible explanations for that: (1) the model is imperfect, (2) the uncertainties of the individual measurements are likely underestimated. Therefore the individual datasets had to be weighed by their inverse scatter around the model curve. This approach is clearly incorrect, but otherwise the influence of the observations which were not obtained with the satellite MOST on the resulting fit would be negligible. There are two solutions presented within Table 9. The first one corresponds to the fit of all available photometric observations and the second one The contribution of component B to the third light is not well-constrained with our data. Various attempts have shown that for a different value of the third light PHOEBE only adjusts the value of the orbital inclination of the system and radii of both components and reaches a solution with comparable χ^2. Therefore it was estimated from the fit of synthetic spectra to the observed ones presented in Table 8 and PHOEBE was allowed to optimize its value slightly. The semimajor axis of orbit 1 was not optimized, because the PHOEBE 1.0 was not designed for modelling the triple systems, hence we were not able to complement the photometric observations with the RVs. The value of the semi-major axis was adjusted after each iteration based on $a_1 \sin i$ given by the fit of the directly measured RVs which is presented in Table 6.

5. Spectro-interferometry

The calibrated visibilities were fitted night-by-night with a model consisting of three uniform disks using the tool LitPro (Tallon-Bosc et al. 2008). The observations obtained in each single night were not sufficient to safely estimate properties of the components of ξ Tau including their position on the plane of

the sky. We needed a model which would account for: (1) the different relative luminosities for each spectral band, and (2) for the presence of two orbits, which mutually bind the positions of individual components together. Neither of these two constraints can be neglected, because the relative luminosities in two spectral bands can differ by $\approx$5% according to the comparison of the synthetic and observed spectra (see Table 8)). If the latter is neglected and the night-by-night approach is used, one would end up with fitting much more parameters than what is necessary. Therefore a simple program which accounts for the two effects was written in Python. The program computes the instantaneous positions of the components projected to the plane of the sky with a following formula:

$$\alpha_i(t) = \arctan\left(\tan\left(v_i(t) + \omega_i(t)\right)\cos I_i\right) + \Omega_i, \quad (6)$$

$$\rho_i(t) = a_i \frac{1 - e_i^2}{1 + e_i \cos v_i(t)} \frac{\cos\left(\omega_i(t) + v_i(t)\right)}{\cos\left(\alpha_i(t) - \Omega_i\right)}, \quad (7)$$

$$x_i = \rho_i \sin \alpha_i, \quad (8)$$

$$y_i = \rho_i \cos \alpha_i, \quad (9)$$

where index i denotes component of a binary, v is the true anomaly, ω is the longitude of periastron, I is the orbital inclination with respect to the plane of the sky, Ω is the position angle of the nodal line, a the angular semimajor axis, e the eccentricity α_i the position angle measured from the North-South direction and ρ_i the angular separation of the two components, (x_i, y_i) are the Cartesian coordinates of a component on the plane of the sky and t is time. The instantaneous value of the length of the periastron is given as follows: $\omega(t) = \omega_0 + k^\omega (t - T_p)$, where T_p is the reference periastron epoch and ω_0 is the value of the longitude of periastron at the periastron epoch. Instead of computing the semimajor axis for each component of a binary, the semimajor axis a and the mass ratio $q = M_1/M_2$ are used; the semimajor axes of primary and secondary can be computed with following formulae: $a_1 = aq/(1 + q)$, $a_2 = a/(1 + q)$. The longitude of periastron of the secondary is $\omega_2 = \omega_1 + \pi$. The centre of mass of the triple system (orbit 2) is placed at the beginning of the Cartesian coordinate system and the centre of mass of the eclipsing binary (orbit 1) is placed at the position of the primary of orbit 2.

Table 9. Light curve solution. (1) Model parameters of a global fit to all available photometric observations, (2) model parameters of a local fit to observations acquired with the satellite MOST.

Solution		(1)		(2)	
Element	Unit		Value		
Orbital properties					
P	(d)	7.1467 ± 0.0001		7.14467 ± 0.000001	
T_p	(RJD)	56224.72426 ± 0.00006		56224.72637 ± 0.00018	
a	(R$_\odot$)	25.46^2		25.46^2	
q		0.9448^1		0.9448^1	
e		0.0^1		0.00224 ± 0.00014	
i	(deg)	87.5315 ± 0.0028		87.7492 ± 0.0014	
ω	(deg)	90		70.07 ± 0.93	
Component properties					
Component		Aa	Ab	Aa	Ab
T_eff	(K)	9700^1	9459.2 ± 1.7	9700^1	9463 ± 2.1
$\log g_\mathrm{[cgs]}$		4.275 ± 0.0000	4.3580 ± 0.0000	4.329 ± 0.0000	4.403 ± 0.0000
Ω		15.5192 ± 0.0039	16.6468 ± 0.0048	15.9200 ± 0.0018	16.8739 ± 0.0020
R	(R$_\odot$)	1.752 ± 0.0000	1.542 ± 0.0000	1.727 ± 0.0000	1.5333 ± 0.0000
L_V		0.1545 ± 0.0027	0.1157 ± 0.0026	–	–
L_B		0.1484 ± 0.0035	0.1103 ± 0.0037	–	–
L_U		0.1185 ± 0.0051	0.0873 ± 0.0050	–	–
L_R		0.18 ± 0.15^3	0.13 ± 0.14^3	–	–
L_M		0.1649 ± 0.0023	0.1235 ± 0.0022	0.16697 ± 0.00021	0.12303 ± 0.00021
Passband luminosity of component B					
L_V^B		0.7299 ± 0.0045		–	
L_B^B		0.7413 ± 0.0059		–	
L_U^B		0.7942 ± 0.0086		–	
L_R^B		0.69 ± 0.24^3		–	
L_M^B		$0.7207s\pm0.0038$		$0.71^1\pm0.0001$	

Notes.
[1] The parameter was kept fixed.
[2] The semimajor axis was not converged, but it was optimized according to a new value of the inclination.
[3] The high uncertainty is caused by insufficient number of observations in the Johnson R band and their poor phase distribution.

Once the positions of all three components are known, objects representing each component can be placed at these positions. For each object the uniform disk was chosen, because all three components are detached and so only minor departures from the spherical symmetry can be expected. The visibility for such model can be computed analytically with a following formula:

$$|V_k(u,v)|^2 = \left| \frac{\sum_{j=1}^{N} L_{j,k} \frac{2J_1(\pi\Theta_j B/\lambda_k)}{\pi\Theta_j B/\lambda_k} e^{-2\pi i(ux_j+vy_j)}}{\sum_{j=1}^{N} L_{j,k}} \right|^2, \quad (10)$$

where index j denotes a component of the triple system, k the spectral band, V the visibility, (u,v) the spatial frequency, L the luminosity fraction, B the length of the baseline, Θ the diameter of the uniform disk, λ the effective wavelength (the central wavelength of the spectra band), J_1 the first-order Bessel function, (x_j, y_j) the Cartesian coordinates of a component computed with the Equation 6, and N the total number of components in the system. The uniform disk diameter Θ is also a wavelength dependent quantity, so a different radius should be derived for each spectral band. Nonetheless the dependency is very weak. The difference between the uniform disk radii in the two filters is of the order of 10^{-3}, i.e. below the accuracy, which one is able to achieve.

The model represented by Equation 10 was fitted to the calibrated squared visibility. The optimal set of parameters was searched by the least squares method, minimizing the following chi-square:

$$\chi^2 = \sum_{k=1}^{N_\mathrm{F}} \sum_{j=1}^{N_\mathrm{O}} \left| \frac{V_k^2(u_j,v_j) - V_{\mathrm{MODEL},k}^2(u_j,v_j)}{\sigma_k(u_j,v_j)} \right|^2, \quad (11)$$

where V^2 is the observed squared visibility, V_{MODEL}^2 the synthetic squared visibility computed with the Equation 10, (u,v) the spatial frequency, σ the standard deviation of the observed squared visibility, N_O the total number of observations of the squared visibility and the N_F the total number of the spectral bands. Equation 11 was minimized with the Sequential Least Squares method (Kraft 1988) implemented within the SciPy scientific library (jon 2001–).

The phase coverage of the inner and the outer orbits is good enough to allow fitting of all orbital elements. However, some elements are better constrained from the spectroscopy and/or photometry, which are available over much longer time intervals than the spectro-interferometry. Those are the orbital periods of the inner orbit P_1 and of the outer orbit P_2, the epoch of the primary minimum of the inner orbit $T_{\mathrm{min},1}$, and the epoch of the periastron passage of the outer orbit $T_{\mathrm{p},2}$. Our early attempts to fit the squared visibility with the model have shown that the the error bars on the individual estimates of the calibrated visibility are underestimated. The χ^2 given by Eq. 11 divided by the degrees of freedom was $\chi_\mathrm{R}^2 \gtrsim 10$. Therefore the error bar of the calibrated visibilities was forced to be greater than 0.05. This step reduced the $\chi_\mathrm{R}^2 \approx 1$. The convergence of each parameter

was inspected and the result of each trial was confronted with the results from the analysis of the spectroscopy and the photometry. The results has shown that the majority of properties of orbit 2, can be fitted and agree well with spectroscopy and the photometry as well as with previous analyses. Except the epoch of the periastron $T_{p,2}$ and the orbital period P_2 all orbital parameters were fitted. The majority of orbital parameters of orbit 1 were unstable and easily converged to implausible solutions. The only two stable parameters, which converged to a plausible solution were the semimajor axis a_1 and the length of the ascending node Ω_1. The diameter of the component B θ_B is stable and can be fitted, diameters of components θ_{Aa} and θ_{Ab} converge to too high values and were estimated from the solution of the light curve no. 2, which is presented in Table 9 and the Hipparcos parallax. Even though the semimajor axis of the orbit 1 is stable, we decided to constrain the parametric space further by employing following condition:

$$a_1 = a_2 \left[\frac{P_2^2}{P_1^2} (1 + q_2) \right]^{-\frac{1}{3}}. \tag{12}$$

This way we take advantage of the semimajor axis of orbit 2 a_2, which is better constrained by our data. The mass ratio of orbit 3 was taken from the fit of the RVs presented in Table 6. The luminosity fractions of the three component were optimized and resulted into values, which were roughly in agreement with the results from the fitting of the synthetic spectra to the disentangled ones. The ratio between components Aa and Ab ($L_{R,Aa}/L_{R,A}$) was oscillating between $\approx 1-3$, so at the end these parameters were estimated from the solution presented in Table 8. The interferometric solution is listed in Table 10 and comparison of the observed and computed squared visibilities is shown in Figure C.1. Two different approaches to estimate the uncertainties of the solution presented in Table 10. The first one was based on the local estimation of the covariance matrix and the second one on a Monte Carlo simulation. The latter also served a test of the robustness of the solution, because all optimized parameters were assigned a uniform a prior probability distribution. Initial parameters for the fitting were randomly drawn from this distribution. Correlations between fitted parameters were studied.

6. Discussion

6.1. Component C

Spectral lines of the fourth component were detected neither via spectral disentangling nor via the comparison with the synthetic profiles. Therefore we estimated the contribution of component C to the total flux from a black-body model to $\approx 1\%$ in the near infrared. The only spectra at our disposal have lower S/N≈ 50 in the infrared region, so the signal of the faintest component is entirely drown in noise.

6.2. Final properties of the system and its components

The sets of parameters defining models which were used throughout this study overlap considerably. As we proceeded through the analyses of the observations based on different methods, we have already used results from one method to constrain the parametric space of another. In some cases it was mandatory, because the solution was degenerated, in other cases it was beneficial, because one of the methods constrained a parameter better. In the following list we justify choice of methods which yield better precision than the remaining ones:

- The spectroscopic elements (K_2, e_2, $T_{\mathrm{periastr.},2}$, P_2, ω_2) of orbit 2 are best defined by the modelling of the RVs given in Table 6. The results from the fitting of RVs were confirmed by disentangling (see Table 7). The χ^2 minimized with KOREL is more complex, because it relies also on the shape of the disentangled spectra. Therefore we expect the direct analysis of the measured RVs to be more reliable.
- The periastron epoch $T_{\mathrm{periatr.,1}}$ and the period P_1 of orbit 1 was obtained with a high precision using the photometry and the direct analysis of the RVs. The photometric solution presented in Table 9 yields the best ephemeris especially thanks to high precision observations from the satellite MOST.
- The eccentricity of orbit 1 is oscillating at the order of 10^{-3} due to dynamic interaction between orbits 1 and 2. A non-zero eccentricity was detected only from the analysis of the observations from the satellite MOST. The precision of the measured RVs and the squared visibilities is not sufficient to confirm this.
- The inclination i_1 of orbit 1 was only determined from the analysis of the photometry. The parameter was not well-constrained by the measured squared visibility and easily converged to an implausible value.
- The luminosity ratios for all three components were estimated from the spectroscopy, photometry spectro-interferometry. The modelling of the light curve has shown that the contribution of component C to the total light is completely correlated with the inclination and component radii, i.e. for any given values of the third light, the minimizer only adjusted the values of the inclination and component radii. The luminosity ratios estimated from modelling of the squared visibilities returned similar values as the other methods, but with much higher uncertainty. The modelling of the disentangled spectra with the synthetic ones provided the most precise luminosity fractions.
- The effective temperatures T_{eff} of both components of orbit 1 are probably better estimated via the comparison of the disentangled profiles and the synthetic spectra. These temperatures were estimated using a spectrum covering an interval of 590 Å, containing many spectral lines, whereas the photometrically determined temperatures would rely on four broad-band filters only. A reliable determination of both temperatures of two almost identical stars from photometry only is virtually impossible (Prša & Zwitter 2006). Nonetheless if the temperatures of components Aa and Ab were both fixed at values from Table 8 the ratio between minima depths was incorrect. Therefore we allowed PHOEBE to optimize also the secondary temperature. Afterwards the secondary temperature sank, but stayed within error bars of the spectroscopic estimate.
- The mass ratio $q_2 = 1.084 \pm 0.006$ of component B and the eclipsing binary, obtained from the analysis of RVs likely has much higher uncertainty than the locally estimated one (see the following section).

At this point each model was re-computed with only those parameters free, which are not better constrained by other measurements and models. A summary of the properties of the triple subsystem based on these final models in Table 11.

6.3. The mass ratio of orbit 2

An attempt to combine the results from the analyses of spectroscopic, photometric and interferometric observations revealed a serious discrepancy. The problem follows:

Table 10. Parameters corresponding to the best-fit of the interferometric observations with the model defined by Eqs 6, 10.

Elements	Units	Values		
		Component properties		
Component		B	Aa	Ab
θ	(mas)	0.438 ± 0.004	0.251^1	0.222^1
L_{BLUE}		0.76^1	0.13^1	0.11^1
L_{RED}		0.72^1	0.16^1	0.12^1
		Orbital properties		
Orbit		2		1
$P_{\mathrm{anomal.}}$	(d)	145.567^1		7.1467^1
$T_{\mathrm{periastr.}}$	(RJD)	55609.05^1		–
$T_{\mathrm{min.I}}$		–		56224.7249^1
a	(mas)	15.63 ± 0.05		1.63 ± 0.02
e		0.215 ± 0.001		0.0^1
q		–		0.96^1
i	(deg)	86.30 ± 0.04		86.3^1
ω	(deg)	7.6 ± 0.2		90.0^1
Ω	(deg)	147.87 ± 0.3		325.3 ± 0.3
k^ω	(deg.yr^{-1})	2.74		–

Notes.
[1] The parameter was kept fixed.

Table 11. Summary of the system based on previous analyses of the spectroscopic, photometric, astrometric and spectro-interferometric observations.

Parameter	Unit	Value		
		Component properties		
Component		B	Aa	Ab
T_{eff}	(K)	13920 ± 460	9700 ± 150	9580 ± 250
$\log g_{[\mathrm{cgs}]}$		4.234 ± 0.080	4.275	4.3580
$v \sin i$	(km s^{-1})	240.6 ± 5.9	23.0 ± 1.0	20.5 ± 1.2
M	(M$_\odot$)	$3.66!^1$	2.232 ± 0.012	2.109 ± 0.011
R	(R$_\odot$)	3.019 ± 0.028^2	1.727 ± 0.001	1.5333 ± 0.001
θ	(mas)	0.439 ± 0.004	0.2541 ± 0.0001^2	0.2224 ± 0.0001^2
		Orbital properties		
Orbit		2		1
$P_{\mathrm{anomal.}}$	(d)	145.567 ± 0.044		7.14665 ± 0.00001
P_{sid}	(d)	145.125 ± 0.044		7.14665 ± 0.00001
$T_{\mathrm{periastr.}}$	(RJD)	55609.05 ± 0.48		–
$T_{\mathrm{min.I}}$	(RJD)	–		56224.7243 ± 0.0002
a	(R$_\odot$)	232.6 ± 1.7		1.847^2
a	(mas)	15.90 ± 0.01		0.0000 ± 0.0000
e		0.2211 ± 0.002		0.0
i	(deg)	86.81 ± 0.01		87.532 ± 0.003
ω	(deg)	187.8 ± 0.5		90.0
Ω	(deg)	148.46 ± 0.01		320.2 ± 0.2
k^ω	(deg.yr^{-1})	2.74 ± 0.30		0.0

Notes.
[1] Estimated assuming orbital inclination $i_2 = 86.81$ deg and the mass ratio $q_2 = 0.85$.
[2] Estimated assuming Hipparcos parallax $\pi = 0.0156 \pm 0.0010$ mas. The parallax was used to estimate the error bar, because it would dominate it completely.

– If the 3-star solution from Table 6 and the solution (1) of the light curve from Table 9 were accepted, the mass of component B would be $M_{\mathrm{B}} = 2.84 \pm 0.04\,\mathrm{M}_\odot$ and the total mass of the eclipsing binary $M_{\mathrm{Aa+Ab}} = 2.62 \pm 0.03\,\mathrm{M}_\odot$.

– If the 3-star solution from Table 6 and the inclination of orbit 2 from analysis of the interferometry were accepted, the inferred mass of component B would be $M_{\mathrm{B}} = 4.71 \pm 0.03\,\mathrm{M}_\odot$.

Given the temperature of component B (see Table 8), the spectral type of this component is B6-7V star whose mass lies within interval of $3.5 - 3.9\,\mathrm{M}_\odot$ (Harmanec 1988). Also the total mass of the eclipsing pair is inconsistent with their spectral type A0V estimated from the spectroscopy. This led us to conclusion that either the inclination or the mass ratio of orbit 2 is not correct.

At first we tested the credibility of the inclination of orbit 2, which was estimated from interferometry. Several large searches

Table 12. A comparison of orbital properties of component B obtained from manually and automatically measured RVs.

Method Element		Automatic	Manual
P_{AN}	(d)	145.567	145.567
T_p	(RJD)	55609.05	55609.05
K	(km s^{-1})	36.87±0.58	39.82±1.25
e		0.207±0.017	0.217±0.034
ω	(deg)	188.3±1.1	191.6±2.2
k^ω	(deg.yr^{-1})	2.75	2.75
rms		2.86	6.13
N		51	51

Fig. 8. A phase plot of the manually measured residua for orbital period $P_R = 0.876$ d and reference epoch T=0.0.

of the parametric space were conducted and their conclusion is that the interferometry is inconsistent with orbital inclination $i_2 \lesssim 80$ deg. This is also supported by the fact that both JN an CH obtained very similar properties of orbit 2, both using their own tools.

Having the inclination verified we focused on the mass ratio q_2 of orbit 2 , which is estimated from the ratio of the semi-amplitudes of the RV curves. Assuming that the masses of components Aa and Ab and the inclination i_2 are correct, the mass ratio of orbit 2 has to be $q_2 = 0.845$. This would also yield mass of component B $M_B = 3.66 \, M_\odot$, which is consistent with the detected spectral type.

The spectral lines of the eclipsing pair are very sharp and they can be measured with precision less than one km s^{-1} (this was verified through a Monte Carlo simulation). Various subsets of the RV measurements on lines of the eclipsing pair were fitted and the results were consistent with the 3-star solution listed in Table 6. Therefore we believe that the resulting elements and especially the semiamplitude K_{Aa+Ab} correspond to the true nature of the triple system.

The component B has very broad and generally shallow lines. Precision of the measurements was roughly three times worse than for the case of lines of eclipsing stars (verified through MC simulation.) To check the validity of the RV measurements obtained via automatic procedure (see Section 3) PH measured RVs of both eclipsing stars using a manual method in which a spectral line is compared with its mirrored profile in program SPEFO (Božić et al. 1995; Horn et al. 1996). RVs of the members of the eclipsing binary were measured on the Mg II 4481 Å spectral line and RVs of component B were measured on Mg II 4481 Å an He I 4471 Å spectral lines. A comparison of the manually and automatically measured RVs is shown in Fig 7. Somewhat surprisingly the automatic procedure systematically detects a lower amplitude of RV of component B and consequently leads to lower semi-amplitude of the best-fit model RV curve, while the measurements on sharp lines of the eclipsing pair are almost the same for both methods. Fits to automatically and manually measured RVs of component B are compared in Table 12. The only fitted elements were the eccentricity, the semiamplitude of the RV curve, the longitude of periastron and the systemic velocity. The semiamplitude of the model RV curve is clearly higher for the manual measuring method, while its rms is more than twice larger than for the RV curve obtained for automatically measured. To investigate this issue we tried to measure RVs of component B using not the disentangled spectra, but synthetic spectra given by parameters in Table 8. A model fitted to these measurements was comparable to those listed in Table 12, but its semiamplitude was only $K_B = 33.29 \pm 0.66$ km s^{-1}. This shows that the semiampli-

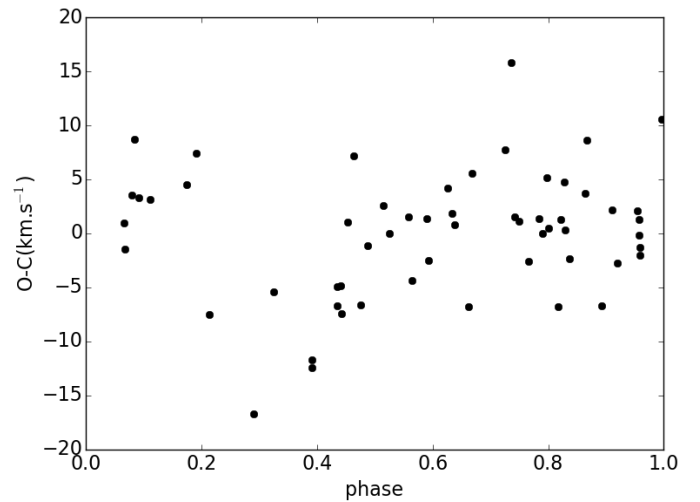tude depends highly on the quality of the chosen template. This may also suggest that this line might be broadened by an additional mechanism, which KOREL is unable to disentangle properly. Nevertheless even the mass ratio resulting from the analysis of manually measured RVs $q_2^{MANUAL} = 0.945$ still predicts too light components of the eclipsing binary.

The relatively high rms can come from the noise and blends. Especially the He I 4471 Å line blends with several metallic lines and has a pronounced non-LTE component. These two effects make the proper estimation of the position of line wings difficult. It is also possible that our model is not correct and there is an unseen fifth companion. This possibility is explored in the next Section.

The mass ratio of orbit 2 can be also estimated from the astrometric solution. The elements from Table 5 imply total mass of the system $M_{TOTAL} = 8.51 \pm 1.70$. The error bars, which come mainly from the uncertainty of the parallax are to generous to provide a reliable estimate.

6.4. A quintuple fairy tale

As already suggested in previous Section, our measurements of RV of component B might be affected by an unseen companion, which causes additional broadening of its spectral lines. The hypothesis is that component B is not a single star, but it is rather a close binary composed of a B-type component and an unseen companion, which distorts the more massive star and that the rapid light variations are actually ellipsoidal variations (see Section 4). The period of the rapid light variations is $P_{R1} = 0.424 \pm 0.005$ d, so the true orbital period is twice $P_R = 0.848 \pm 0.10$.

A search for this period was conducted in residuals of the RV curve fit for both manually and automatically measured RVs. A period of one day was found in residuals of automatically measured RVs, but a period $P_R = 0.876$ d was found in residuals of the manually measured RVs. A phase plot of the RV curve is shown in Figure 8. An attempt to fit the radial velocity curve, assuming that the component B is a member of a close binary and semiamplitude of its radial velocity curve is $K_B = 44.5$ km s^{-1} returned a model with semiamplitude $K_R = 4.7 \pm 1.8$ km s^{-1}. The fit is shown in Figure 9.
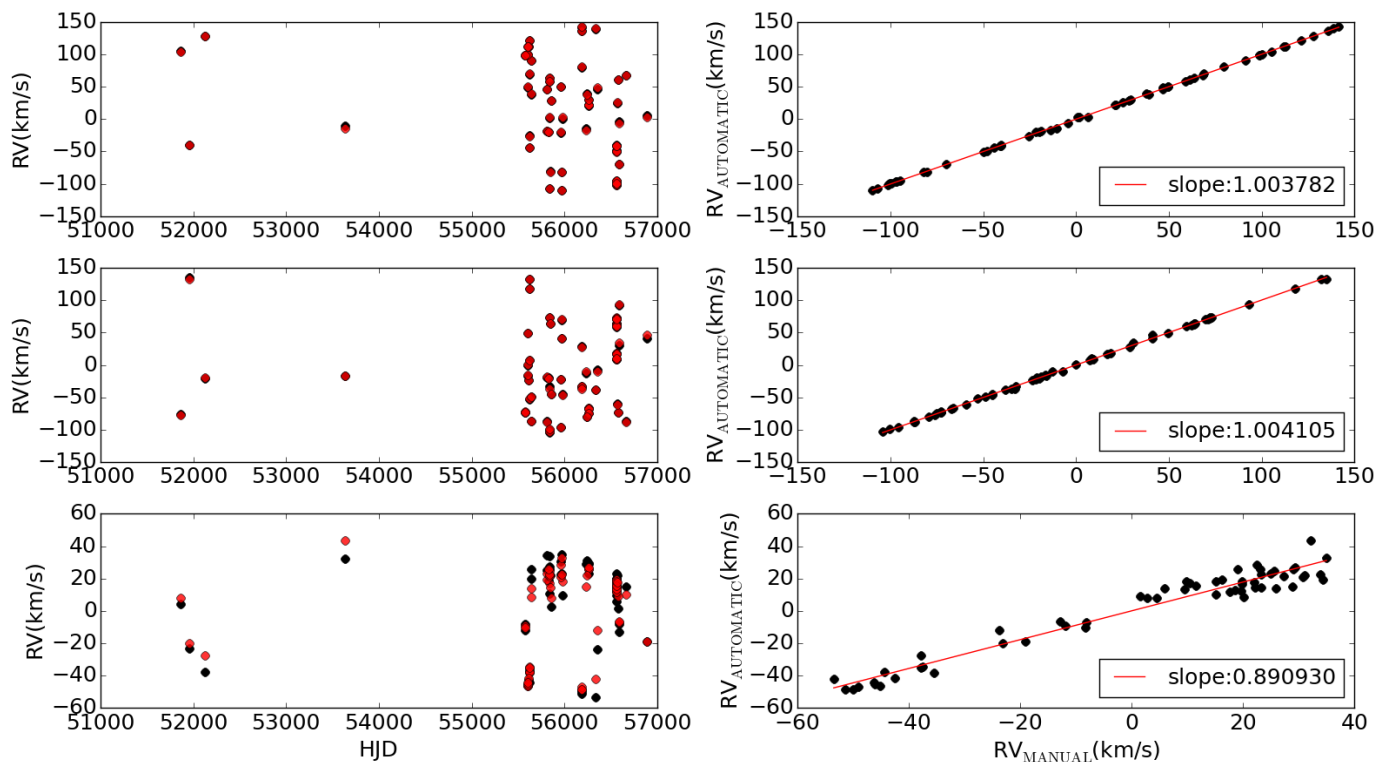
Fig. 7. Comparison of manually (black) and automatically (red) measured RVs of ξ Tau. The components are following Aa - top panel, Ab - middle panel, B - bottom panel. Left panels - RVs vs. time, right panels - RVs(Manual) vs. RVs(Automatic). The dependency was fitted with a linear function (red line). Its slope is given in the legend.

Following properties of the orbit (denoted with subscript R) can be estimated: 1) The binary orbit is very likely circular due to small distance between the components. 2) The orbital period and the semiamplitude of the 0.876 d orbit imply mass function $f(m)_{\rm R} = 9.42.10^{-6}$. 3) Adopting the primary mass $M_{\rm B} = 3.66\,{\rm M}_\odot$ and an inclination one can estimate the mass ratio, the secondary mass and the semimajor axis. A search for an inclination, which would generate ellipsoidal variations comparable to the detected ones was conducted. The model was computed with the program PHOEBE and the inclinations within the interval $I = [15, 30]$ deg generate ellipsoidal variation which agree with the amplitude of the detected rapid light variations (see Section 4). An illustrative comparison for following elements of the rapid orbit is shown in Figure 10: $P_{\rm R} = 0.848$ d, $i_{\rm R} = 20$ deg, $q_{\rm R} = 0.041$, $a_{\rm R} = 6.02\,{\rm R}_\odot$, and the secondary mass $M_{\rm Bb} = 0.151$, which would be a late M-type star. Main sequence radii of both stars were assumed and third light coming from the eclipsing binary was also taken into account. It should be pointed out that this hypothesis suffers from a few discrepancies: 1) The best fit solution of the manually-measured RVs of component B yields the semiamplitude $K_{\rm B} = 40$ km s^{-1}. The one with $K_{\rm B} = 44.5$ km s^{-1} has χ^2 approximately 20% higher than the former one. Therefore the discrepant mass ratio of orbit 2 cannot be explained by the additional motion of the component B in the 0.876 d orbit. 2) The observed light curve does not indicate any periodical variations of its depth. 3) Fine structure and variations of the period of the light variations are not explained by the model curve. The variations of the orbital motion may arise from tidal interaction of the two components. 4) A simulation which would confirm/disprove stability of such configuration is desirable.

6.5. Dynamic effects in the system

This section will be done once we accept a final model of component B.

6.6. Comparison with models of stellar evolution

This section will be done once we accept a final model of component B.

7. Conclusion

References

2001–, SciPy: Open source scientific tools for Python, [Online; accessed 2015-01-20]
Bolton, C. T. & Grunhut, J. H. 2007, in IAU Symposium, Vol. 240, IAU Symposium, ed. W. I. Hartkopf, P. Harmanec, & E. F. Guinan, 66
Bonneau, D., Clausse, J.-M., Delfosse, X., et al. 2006, A&A, 456, 789
Borkovits, T., Érdi, B., Forgács-Dajka, E., & Kovács, T. 2003, A&A, 398, 1091
Božić, H., Harmanec, P., Horn, J., et al. 1995, A&A, 304, 235
Butterworth, S. 1930, Wireless Engineer, 7
Campbell, W. W. 1909, Astrophysical Journal, 29, 224
Claret, A. 1998, A&AS, 131, 395
Claret, A. 2001, MNRAS, 327, 989
de Laverny, P., Recio-Blanco, A., Worley, C. C., & Plez, B. 2012, A&A, 544, A126
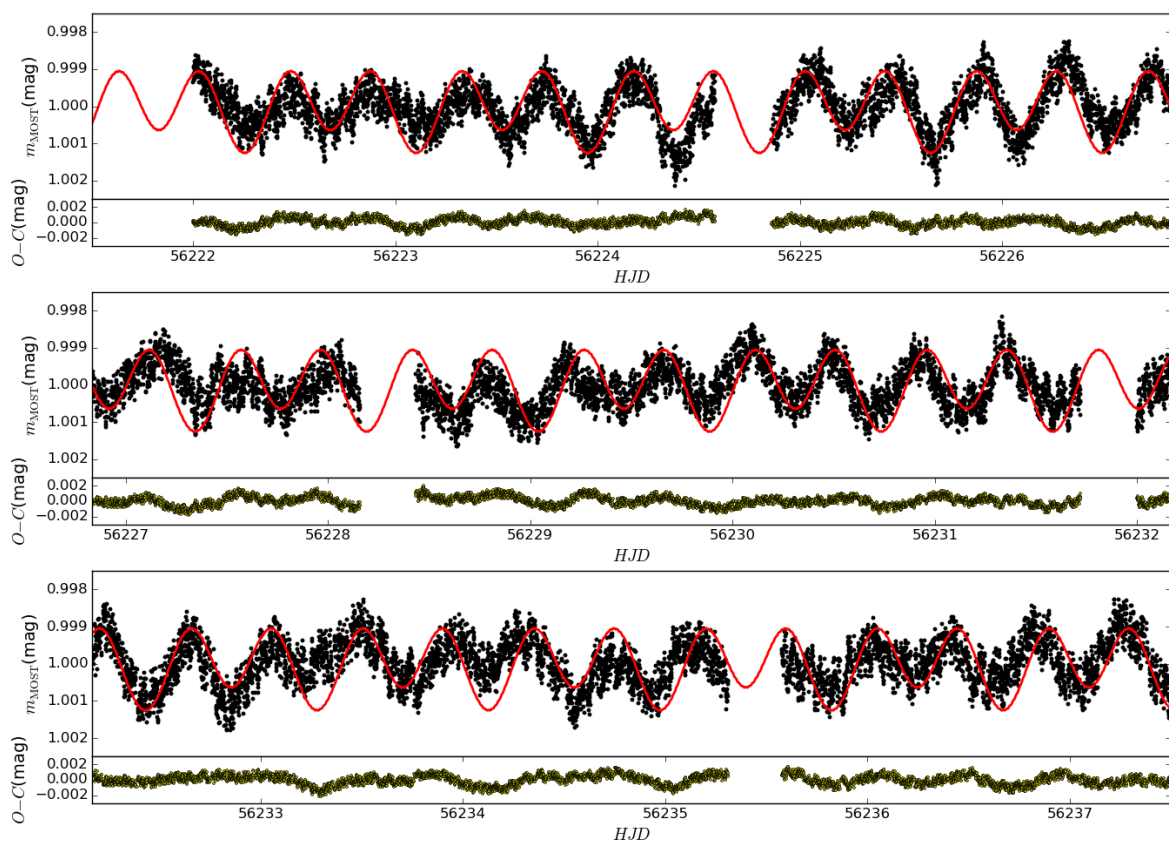
Fig. 10. Comparison of the light curve from the satellite MOST with a model of ellipsoidal variations generated by the motion of component B in a very close 0.876 d binary with a much less massive secondary. The observations are denoted with black points, the model light curve with a red line and residuals with yellow colour.

Fekel, J. F. C. 1981, ApJ, 246, 879

Hadrava, P. 1995, A&AS, 114, 393

Hadrava, P. 1997, A&AS, 122, 581

Hadrava, P. 2009, ArXiv e-prints

Harmanec, P. 1988, Bulletin of the Astronomical Institutes of Czechoslovakia, 39, 329

Harmanec, P. 1998, A&A, 335, 173

Harmanec, P., Koubský, P., Nemravová, J. A., et al. 2015, A&A, 573, A107

Horn, J., Kubat, J., Harmanec, P., et al. 1996, A&A, 309, 521

Hummel, C. A., Zavala, R. T., & Sanborn, J. 2013, Central European Astrophysical Bulletin, 37, 127

Kaufer, A., Stahl, O., Tubbesing, S., et al. 1999, The Messenger, 95, 8

Kirkpatrick, S., Gelatt, C. D., & Vecchi, M. P. 1983, Science, 220, 671

Kraft, D. 1988, A software package for sequential quadratic programming, Deutsche Forschungs- und Versuchsanstalt für Luft- und Raumfahrt Köln: Forschungsbericht (Wiss. Berichtswesen d. DFVLR)

Lafrasse, S., Mella, G., Bonneau, D., et al. 2010, VizieR Online Data Catalog, 2300, 0

Lenz, P. & Breger, M. 2004, in IAU Symposium, Vol. 224, The A-Star Puzzle, ed. J. Zverko, J. Ziznovsky, S. J. Adelman, & W. W. Weiss, 786–790

Mason, B. D., Martin, C., Hartkopf, W. I., et al. 1999, AJ, 117, 1890

Mason, B. D., Wycoff, G. L., Hartkopf, W. I., Douglass, G. G., & Worley, C. E. 2001, AJ, 122, 3466

Moultaka, J., Ilovaisky, S. A., Prugniel, P., & Soubiran, C. 2004, PASP, 116, 693

Mourard, D., Clausse, J. M., Marcotto, A., et al. 2009, Astronomy and Astrophysics, 508, 1073

Nasseri, A., Chini, R., Harmanec, P., et al. 2014, A&A, 568, A94

Nelder, J. A. & Mead, R. 1965, The Computer Journal, 7, 308

Nemravová, J. A., Harmanec, P., Bencheikh, J., et al. 2013, Central European Astrophysical Bulletin, 37, 207

Palacios, A., Gebran, M., Josselin, E., et al. 2010, A&A, 516, A13

Prša, A. & Zwitter, T. 2005, ApJ, 628, 426

Prša, A. & Zwitter, T. 2006, Ap&SS, 304, 347

Rappaport, S., Deck, K., Levine, A., et al. 2013, ApJ, 768, 33

Rica Romero, F. M. 2010, Rev. Mexicana Astron. Astrofis., 46, 263

Simon, K. P. & Sturm, E. 1994, A&A, 281, 286

Steiner, I., Stahl, O., Seifert, W., Chini, R., & Quirrenbach, A. 2008, in Society of Photo-Optical Instrumentation Engineers (SPIE) Conference Series, Vol. 7014, Society of Photo-Optical Instrumentation Engineers (SPIE) Conference Series, 4

Stellingwerf, R. F. 1978, ApJ, 224, 953

Tallon-Bosc, I., Tallon, M., Thiébaut, E., et al. 2008, in Society of Photo-Optical Instrumentation Engineers (SPIE) Conference Series, Vol. 7013, Society of Photo-Optical Instrumentation Engineers (SPIE) Conference Series

ten Brummelaar, T. A., McAlister, H. A., Ridgway, S. T., et al. 2005, ApJ, 628, 453

Tokovinin, A. A. 1997, A&AS, 124, 75

van Leeuwen, F. 2007, A&A, 474, 653

Walker, G., Matthews, J., Kuschnig, R., et al. 2003, PASP, 115, 1023

Zasche, P., Uhlar, R., Kucakova, H., Svoboda, P., & Masek, M. 2014, Information Bulletin on Variable Stars, 6114, 1
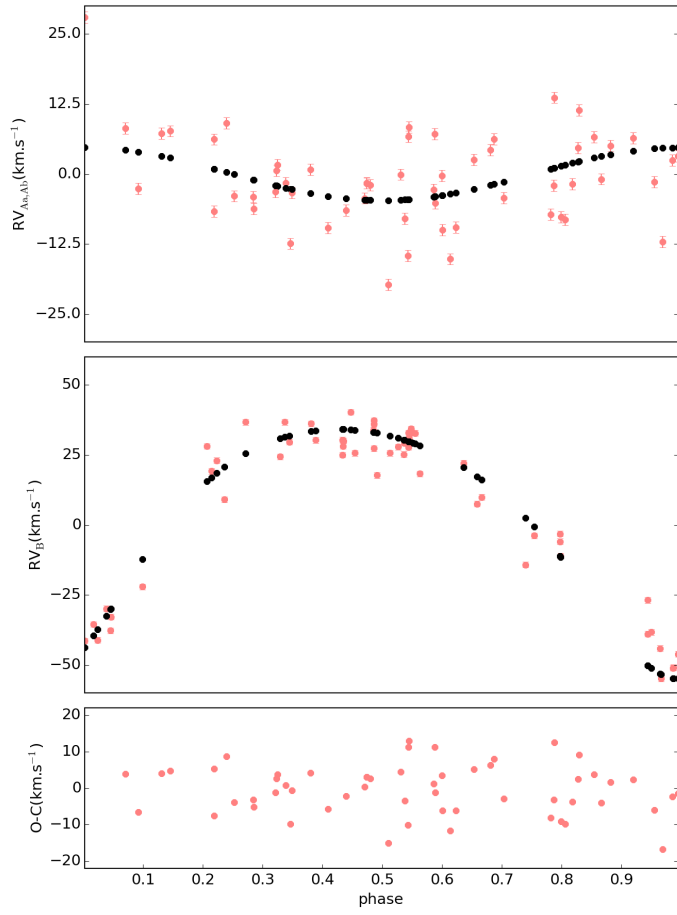
Fig. 9. A fit to the manually (see 6.4 for details) measured RVs of component B. It is assumed that component B is a member of a close binary. Top panel - the close orbit with period $P_{\mathrm{R}} = 0.876\,\mathrm{d}$. Middle panel - orbit 2.

Appendix A: Details on spectroscopic data sets

Appendix B: Details on photometric data sets

Here, we provide some details on the photometric observations.
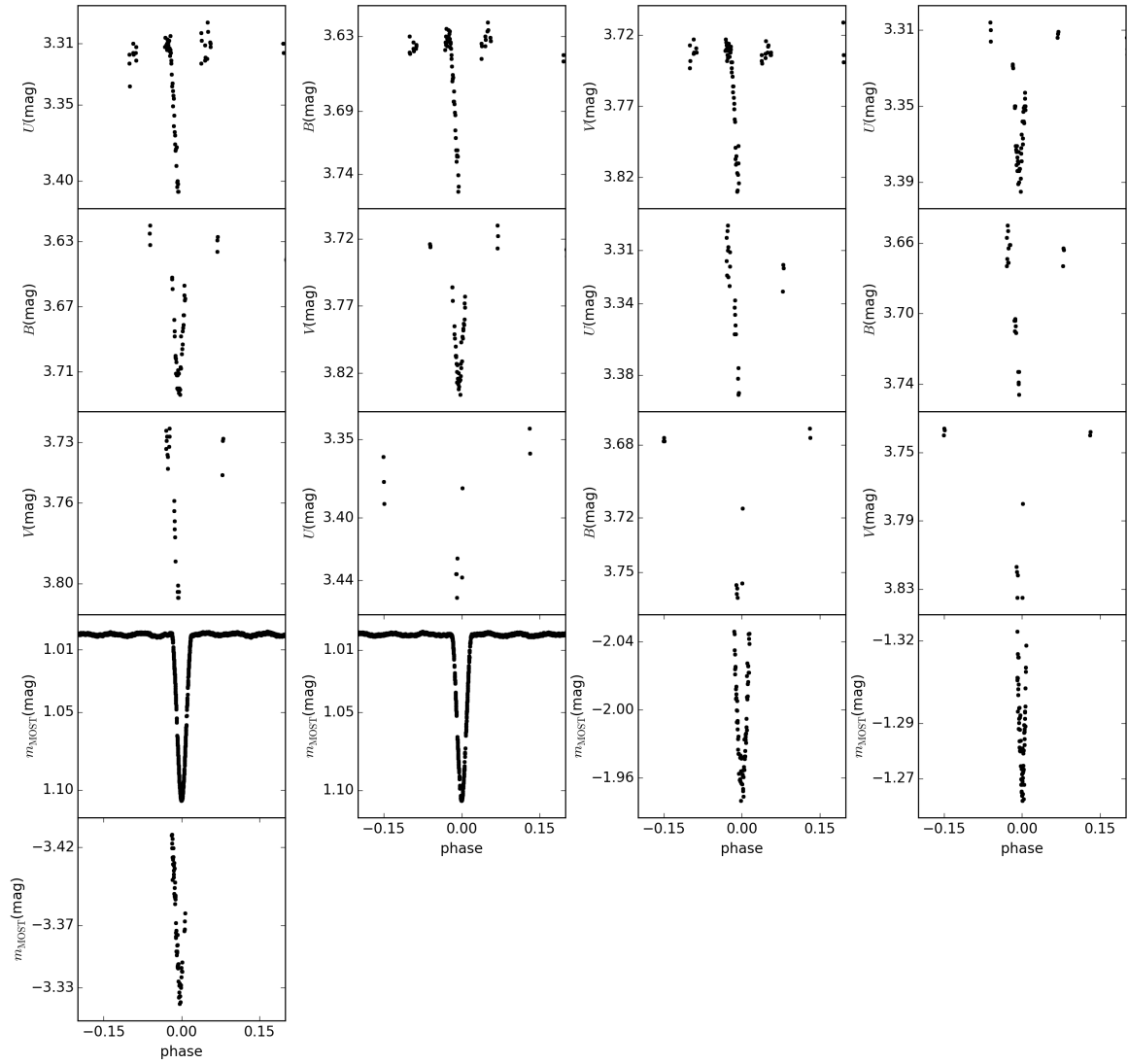
Appendix C: Interferometric fits

Fig. B.1. All available primary minima of orbit 1. The filters are denoted as follows: UBV - Johnson's UBV filters, m_{MOST}, the filter of the satellite MOST.
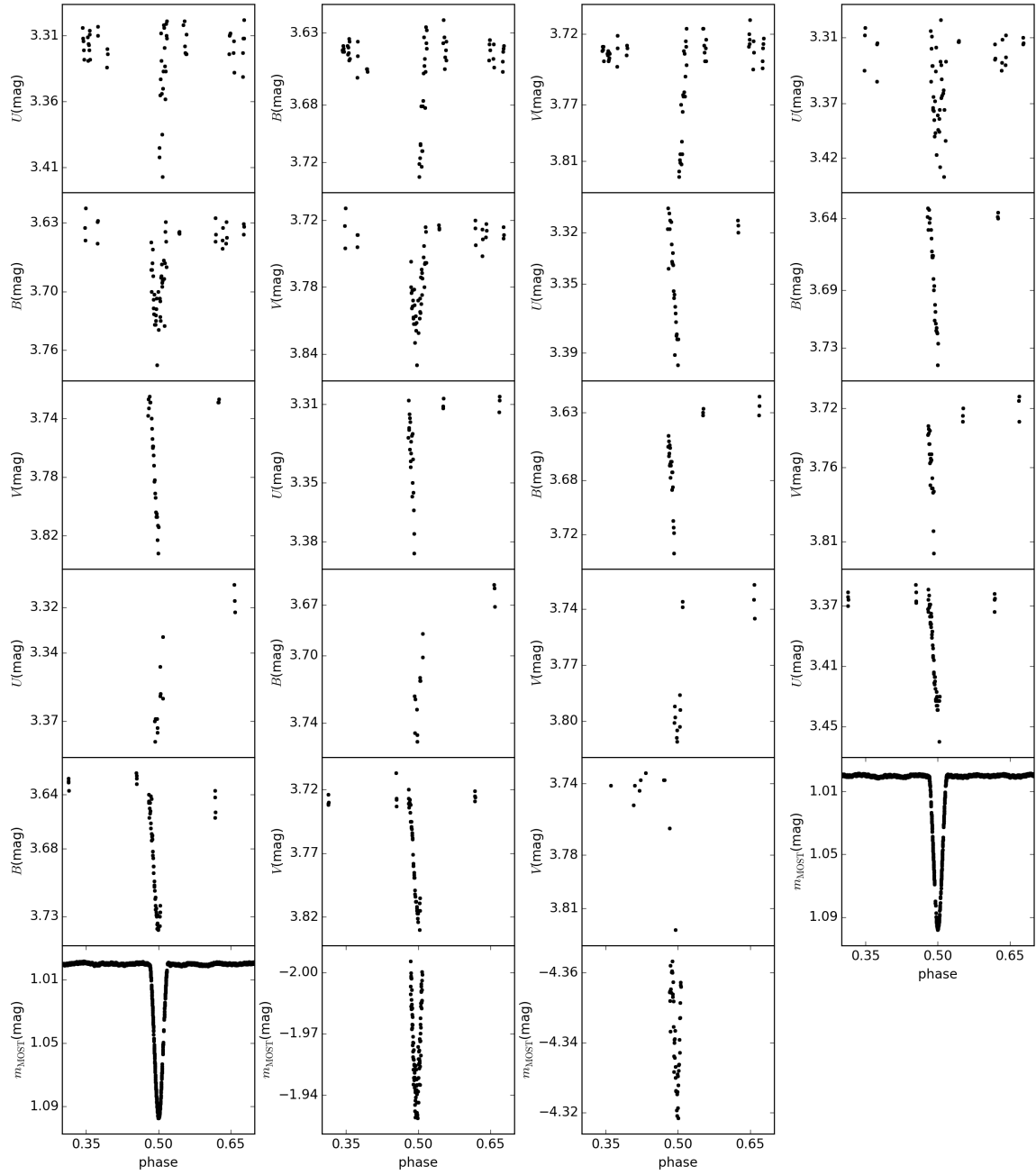
Fig. B.2. All available secondary minima of orbit 1. The filters are denoted as follows: UBV - Johnson's UBV filters, m_{MOST}, the filter of the satellite MOST.
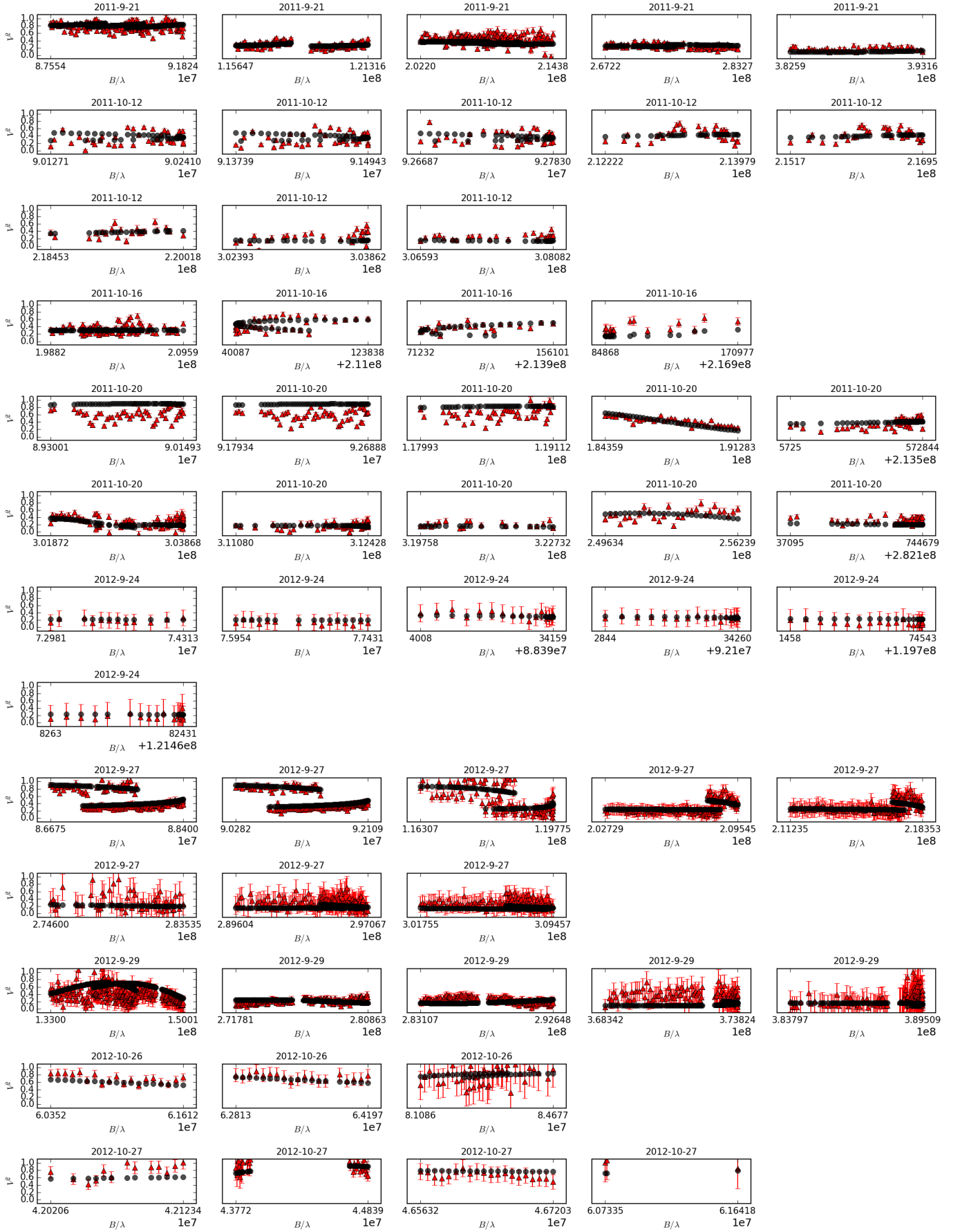
Fig. C.1. Fit of the orbital model to the CHARA/VEGA spectro-interferometric observations. Black points denote model defined by Eqs 6, 10, red points the calibrated squared visibilities. The night during which the data were recorded is given in format YYYY.MM.DD above each panel.